J. Fluid Mech. (1999), *vol.* 394, *pp.* 303–337. Printed in the United Kingdom

Three-dimensional structure and momentum transfer in a turbulent cylinder wake

By A. VERNET[1], G. A. KOPP[2], J. A. FERRÉ[1] AND FRANCESC GIRALT[1]

[1] Escola Tecnica Superior d'Enginyeria Quimica, Universitat Rovira i Virgili, Carretera de Salou, s/n, 43006 Tarragona, Catalunya, Spain

[2] Boundary Layer Wind Tunnel Laboratory, Faculty of Engineering Science, The University of Western Ontario, London, Ontario, N6A 5B9, Canada

(Received 20 May 1998 and in revised form 9 April 1999)

Simultaneous velocity and temperature measurements were made with rakes of sensors that sliced a slightly heated turbulent wake in the spanwise direction, at different lateral positions 150 diameters downstream of the cylinder. A pattern recognition analysis of hotter-to-colder transitions was performed on temperature data measured at the mean velocity half-width. The velocity data from the different 'slices' was then conditionally averaged based on the identified temperature events. This procedure yielded the topology of the average three-dimensional large-scale structure which was visualized with iso-surfaces of negative values of the second eigenvector of $[\boldsymbol{S}^2 + \boldsymbol{\Omega}^2]$. The results indicate that the average structure of the velocity fluctuations (using a triple decomposition of the velocity field) is found to be a shear-aligned ring-shaped vortex. This vortex ring has strong outward lateral velocities in its symmetry plane which are like Grant's mixing jets. The mixing jet region extends outside the ring-like vortex and is bounded by two foci separated in the spanwise direction and an upstream saddle point. The two foci correspond to what has been previously identified in the literature as the double rollers.

The ring vortex extracts energy from the mean flow by stretching in the mixing jet region just upstream of the ring boundary. The production of the small-scale (incoherent) turbulence by the coherent field and one-component energy dissipation rate occur just downstream of the saddle point within the mixing jet region. Incoherent turbulence energy is extracted from the mean flow just outside the mixing jet region, but within the core of the structure. These processes are highly three-dimensional with a spanwise extent equal to the mean velocity half-width.

When a double decomposition is used, the coherent structure is found to be a tube-shaped vortex with a spanwise extent of about $2.5l_0$. The double roller motions are integral to this vortex in spite of its shape. Spatial averages of the coherent velocity field indicate that the mixing jet region causes a deficit of mean streamwise momentum, while the region outside the foci of the double rollers has a relatively small excess of streamwise momentum.

1. Introduction

The importance of three-dimensional large-scale turbulence structures in fully developed turbulent flows has been known since the pioneering work of Theodorsen (1952), Townsend (1956) and Grant (1958). Theodorsen predicted that the predomi-

nant structure in turbulence should be a horseshoe-like vortex while Townsend and Grant, from an analysis of correlation measurements, inferred two dominant structures, namely double rollers and mixing jets. Flow visualization has also helped to establish the existence of far-wake structures (e.g. Taneda 1959; Keffer 1965; Cimbala, Nagib & Roshko 1988) although it gave little information about their topology.

The large-scale structures in far wakes have been identified with several techniques (e.g. Payne & Lumley 1967; Mumford 1983; Antonia *et al.* 1987; Ferré & Giralt 1989*a*, *b*; Hayakawa & Hussain 1989; Ferré *et al.* 1990; Gieseke & Guezennec 1993; Kopp, Kawall & Keffer 1995; Vernet *et al.* 1997). Payne & Lumley used proper orthogonal decomposition with the correlation data of Grant to refine some details regarding the double roller structure. Following this line of research, Mumford (1983) used pattern recognition to identify double and single roller structures with simultaneous multiple sensors. Ferré & Giralt (1989*a*, *b*) enhanced the pattern recognition technique, and on the basis of separate measurements in the horizontal (homogeneous) and vertical (shear) planes, they speculated on the existence of horseshoe-like structures (Ferré *et al.* 1990; Giralt & Ferré 1993). By using simultaneous temperature and velocity sensors, Vernet *et al.* (1997) gave further evidence that Townsend's and Grant's double roller and mixing jet structures are different aspects of a single structure, probably a horseshoe-shaped structure.

Antonia *et al.* (1987) used events in the passive temperature field to identify structures in a single vertical plane. In particular, they utilized five temperature probes placed in a homogeneous (x, z) plane near the location of maximum shear and selected events containing temperature 'fronts' in all five signals simultaneously. With this technique they investigated the transfer processes pertaining to vortices occurring in an alternating mode and found significantly different results when compared to those in the near-wake region. Continuing along this line, Bisset, Antonia & Browne (1990) also identified the motions in the shear (vertical) plane associated with structures in alternating and symmetric modes. Using a kinematic model of the far wake based on a vortex array they found that the motions in the shear plane are consistent with a double roller structure in homogeneous (x, z) planes. Kopp *et al.* (1995) also found strong evidence for horseshoe (what they called Λ-shaped) vortices by comparing results from rapid distortion theory applied to a kinematic model of Λ-vortices and a pattern recognition analysis of experimental data from a uniformly distorted plane turbulent wake.

These structures exist over a wide range of Reynolds numbers, from $Re \sim 10^3$ in the experiments by Antonia's group to about $Re \sim 10^4$ in the experiments at Tarragona. They could be expected to exist up to $Re \sim 10^5$ since the drag coefficient remains constant over this range.

Theodorsen (1952), Ferré *et al.* (1990) and Giralt & Ferré (1993) argued that horseshoe structures are important because they maintain the correlation between the streamwise and lateral velocity fluctuations (i.e. the Reynolds shear stress) and thus should play an important role in the momentum transfer. They point out that, because the wake is controlled by a single length scale due to the double roller/horseshoe structure, a simple eddy viscosity model generally works well once the intermittency at the edges of the wake is taken into account (Libby 1976), i.e.

$$-\overline{uv} = v_t \frac{\mathrm{d}\overline{U}}{\mathrm{d}y}. \tag{1}$$

The origin of far-wake coherent structures has been a somewhat contentious issue with two opposing points of view, namely (i) that these structures are created by the

linear instability of the mean velocity profile in the far wake, or (ii) that they evolve directly from the Kármán vortices in conjunction with secondary structures, called 'ribs', which link adjacent Kármán vortices. The experiments of Wygnanski, Champagne & Marasli (1986) indicated that there is a lack of 'universal' self-preservation and that the mean velocity profile is universal in shape only. In addition, they showed that a linear inviscid stability analysis can predict the general form of the far-wake structures, but that the precise details depend on the initial geometry and possibly on the initial coherent structures. Cimbala *et al.* (1988) argued, however, that the far-wake structures do not depend on the initial vortices, neither their scale nor frequency, but depend rather on the instability of the mean velocity profile. In contrast, Meiburg & Lasheras (1988) and Hayakawa & Hussain (1989) show how the far-wake coherent structures, in the shape of a horseshoe, may evolve from the Kármán vortices and streamwise vortices called 'ribs', which are believed to connect adjacent Kármán vortices.

What all of the previous studies have in common is that they relied on two-dimensional data to infer the existence of the three-dimensional structure and the possible effects of such a structure on the transfer processes within the wake and across the turbulent–non-turbulent interface. In the present work, three-dimensional data are obtained by utilizing the temperature field in the same manner as Vernet *et al.* (1997) so that the three-dimensional structure and its related transfer processes are unambiguously identified.

The objective of this paper is to identify and visualize the average three-dimensional large-scale structure in the far wake from simultaneous velocity and temperature measurements and to establish its relationship with the transport of momentum and turbulence energy. We will not deal directly with the origin of the structures. In § 2 we describe the experimental setup while in § 3 we present the identification technique which utilizes pattern recognition on the temperature field to conditionally average the simultaneously measured velocity field. The topology of the prototypical structure in the velocity fluctuations, identified via the transitions from hotter-to-colder fluid motions in the passive temperature field, is discussed in § 4. In § 5, the 'shape' of the coherent structure, and whether or not it is a vortex, are discussed. The three-dimensional topology of the turbulence production and dissipation associated with the coherent structure is discussed in § 6. Finally, the conclusions are summarized in § 7.

2. Experimental details

Measurements in a plane turbulent cylinder wake were made in the open return wind tunnel at Universitat Rovira i Virgili in Tarragona. This facility has a test section 60×60 cm square and 300 cm long. The diameter of the cylinder, D, was 12 mm (aspect ratio of 50 and tunnel blockage of 2.0%) while the free-stream velocity, U_0, was $9\,\mathrm{m\,s^{-1}}$, so that the Reynolds number was 7000. The free-stream turbulence intensity was less than 0.2%. The cylinder, which was mounted through holes in the tunnel walls, was fitted with an electrical resistance of $50\,\Omega$ which provided a maximum mean temperature excess of 0.8 K at $x/D = 150$.

A rake of four resistance thermometers (cold wires) spanning the homogeneous Z^*-direction in steps of $0.56l_0$ was positioned at the downstream location $x/D = 150$ and $Y^* = 1.0$, as shown in figure 1. The spatial coordinates are normalized according to $Z^* = z/l_0$, $Y^* = y/l_0$ and $X^* = -U_0 t/l_0$, where $y = l_0 = 50$ mm is the lateral location where the mean velocity defect is half of its maximum value. The conversion of the time coordinate to the streamwise coordinate requires the use of Taylor's hypothesis

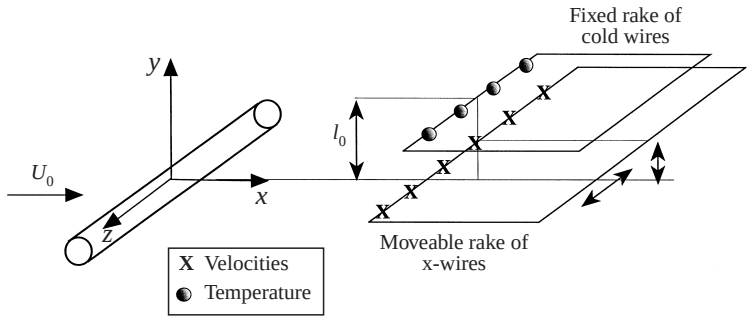

FIGURE 1. Definition sketch.

of frozen turbulence. The far wake is well-suited to this hypothesis because of the relatively high convection velocities of the coherent structures. For example, Antonia *et al.* (1987) found a convection velocity of $0.97U_0$ at $x/D = 420$ while in the present work a slightly lower value of $0.95U_0$ is used because of the closer proximity to the cylinder. Note that the free-stream velocity is used for the conversion of time into the streamwise coordinate throughout this paper.

A rake of six X-wires, with probes separated by $0.28l_0$, was placed parallel to the cold wires. This rake, which could be moved both in the spanwise (Z^*) and lateral (Y^*) directions, was located at 12 different lateral Y^*-locations ranging from $-0.5 < Y^* < 2.25$ and at three different spanwise Z^*-locations. One of the X-wires was overlapped when the rake was moved in the spanwise direction, so that on all plots $(6 \times 3 - 2) = 16$ sensors are shown in the Z^*-direction. The X-wires themselves were oriented in two different configurations at each location in order to measure either the streamwise and lateral velocity components or the streamwise and spanwise components. In total, $(12 \times 3 \times 2) = 72$ data files were obtained and stored. Thus, (u, v) and (u, w) data were obtained at $(12 \times 16) = 192$ points in the (y, z)-plane at $x/D = 150$. This compares with the extensive measurements made by Guezennec (1989) in a turbulent boundary layer with $(13 \times 11) = 143$ points per plane normal to the direction of flow at eight streamwise locations. In contrast, the present measurements were made at a single streamwise location with streamwise variations being accounted for by Taylor's hypothesis.

The voltage signals from each anemometer were low-pass filtered at 2 kHz and sampled at 5000 samples/s for 40 s (0.2 ms between samples). The data were stored on optical disks. Note that no data were obtained on the other side of the wake because previous measurements with the present technique revealed neither alternating nor symmetric modes when the structures on one side of the wake were identified without considering the other side. (This fact can also be observed in the results of Giralt & Ferré 1993 in their figure 2.) Note also that 40 s provides sufficient data for convergence of the statistics described later in the text since during this time we are able to identify over 500 structures.

The present analysis is generally based on fluctuations from the time mean. The streamwise, lateral and spanwise velocity fluctuations $\tilde{u}$, $\tilde{v}$, and $\tilde{w}$, respectively, are normalized with the maximum mean velocity defect ($U_s = 1.0\,\mathrm{m\,s^{-1}}$) at $x/D = 150$. Thus, $u^* = \tilde{u}/U_s$, $v^* = \tilde{v}/U_s$ and $w^* = \tilde{w}/U_s$. (Exceptions to this are explicitly noted in the text.) The temperature fluctuations are normalized by the local r.m.s. value, namely $\theta^* = \tilde{\theta}/\theta'$. In addition, $\overline{U}$, $\overline{V}$ and $\overline{W}$ are the mean streamwise, lateral and spanwise velocities, respectively, with $U^* = \overline{U}/U_s$, $V^* = \overline{V}/U_s$ and $\overline{W} = 0$. The

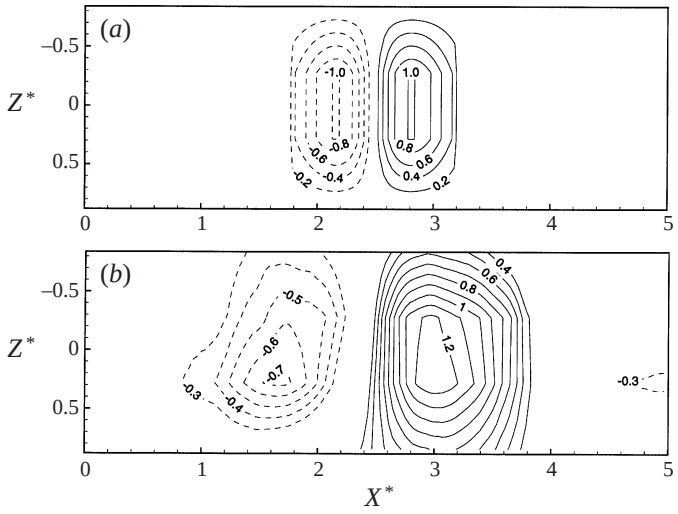

FIGURE 2. Isocontours of (*a*) the initial template depicting the hotter-to-colder temperature transition and (*b*) the resulting ensemble average of $\langle\theta^*\rangle$ in the (X^*, Z^*)-plane at $Y^* = 1.0$.

streamwise r.m.s. velocity at $Y^* = 1.0$ is $u_0' = 0.23\,\mathrm{m\,s^{-1}}$ while $\theta_0' = 0.15\,\mathrm{K}$. These values are 0.25 and 0.13 at $Y^* = 0$, respectively. The maximum value of u' is $0.27\,\mathrm{m\,s^{-1}}$ and occurs at $Y^* = 0.6$. Taylor's integral scale is 8.1 ms ($\simeq 1.5 l_0$).

3. Identification of the prototypical coherent structure

3.1. *Decomposition and averaging techniques*

There have been typically two different decompositions of the velocity field used in conjunction with the identification of coherent structures, namely the double and triple decompositions. In the triple decomposition, the total instantaneous velocity, u, is the sum of the mean, $\overline{U}$, the coherent velocity, u_c, and the incoherent velocity fluctuation, u_r, such that

$$u_i(x, y, z, t) = \overline{U}_i(x, y) + u_{c,i}(x, y, z, t) + u_{r,i}(x, y, z, t), \tag{2}$$

where the coherent velocity, u_c, is the ensemble average of the difference between the total and mean velocities, i.e. $u_c = \langle u - \overline{U}\rangle$ (e.g. Hussain 1983; Antonia *et al.* 1987). The angular brackets indicate the ensemble average and the subscripts c and r are not indices but signify the coherent and incoherent components. The index, i, represents the three coordinate directions x, y and z.

In the present work we have not measured the x-dependence explicitly, but have relied on Taylor's hypothesis to convert our time-based measurements to spatial x. The assumption of Taylor's hypothesis implies that the structure does not change as it passes the set of probes. This also means that the explicit time dependence of the structures is not a factor if all structures included in the average are of roughly the same 'age'. Therefore, the total instantaneous velocity in the far region of the plane wake is decomposed as

$$u_i(x, y, z, t) = \overline{U}_i(x, y) + u_{c,i}(x, y, z) + u_{r,i}(x, y, z, t). \tag{3}$$

Two additional points should be noted. First, this decomposition is similar to Reynolds' decomposition in that the instantaneous velocity fluctuation, $\tilde{u}$, is equal to

the sum of the coherent and incoherent velocities. Thus, the incoherent (also called 'small-scale' or 'random') velocity is the difference between the instantaneous velocity fluctuation and the coherent velocity,

$$u_{r,i}(x, y, z, t) = \tilde{u}_i(x, y, z, t) - u_{c,i}(x, y, z). \tag{4}$$

Second, this notation differs slightly from that of Hussain (1983).

In the double decomposition, the total instantaneous velocity is decomposed as

$$u_i(x, y, z, t) = U_{conv}(x) + u_{c2,i}(x, y, z) + u_{r,i}(x, y, z, t), \tag{5}$$

where U_{conv} is a suitably chosen convection velocity and $u_{c2} = \langle u - U_{conv} \rangle$. In plane wakes U_{conv} is typically taken as a function of x, although Zhou & Antonia (1992) point out that it is also a function of y so that vortices located away from the average location move at a slightly different speed.

In the double decomposition, the mean shear is accounted for by the coherent (ensemble-averaged) motions while for triple decompositions it is not. Thus, the ensemble averages from the double and triple decompositions are not the same. They are related, however. Presuming that u_r is the same with both decompositions (this must be true when the event selection is not based on the velocity field), then

$$u_{c2} = u_c + \overline{U} - U_{conv}. \tag{6}$$

Therefore, the ensemble average from the double decomposition can be obtained from the triple decomposition by adding the local mean and subtracting the convection velocity from the coherent velocity.

3.2. *Pattern-recognition technique*

The pattern-recognition (PR) technique involves cross-correlating an initial template $a(z;t)$ with, in this case, the temperature data $\theta(x, y, z; t + \tau)$ sampled during an experiment. With the temperature rake fixed at $x/D = 150$ and $Y^* = 1.0$, $\theta = \theta(z; t + \tau)$, the cross-correlation is given by

$$\gamma(\tau) = \frac{\overline{a(z;t)\theta(z;t+\tau)}}{a'\theta'}. \tag{7}$$

The overbar in this equation indicates an average over z and t, where the z-range is the number of temperature sensors and t is the number of data points in time (which is converted to X^* via Taylor's hypothesis). In the present study $\gamma(\tau)$ is calculated for time lags up to $\tau = 40$ s (i.e. for the entire data set).

A hotter-to-colder temperature transition, shown in figure 2(*a*), has been used as the initial template to analyse the temperature field recorded simultaneously with the velocity data. Values of the cross-correlation coefficient, $\gamma(\tau)$, larger than a threshold level (selected here to be the 1.5 times the r.m.s. value, γ', of the cross-correlation) identify the occurrence of individual events similar to the temperature template. These events are ensemble averaged with the current ensemble average being used as the template for the next iteration. This procedure is repeated until the new template (i.e. ensemble average) is equal to the penultimate template. The process of iteration removes the bias that may be introduced through the selection of the initial temperature template or pattern (see the Appendix). In the present work, four iterations were required for convergence of the temperature pattern given in figure 2(*b*). Further details regarding the PR technique can be found in Ferré & Giralt (1989*a*, *b*) and Kopp, Ferré & Giralt (1997). Effects of the choice of template are investigated in the Appendix where it is found that three significantly different

temperature templates yield similar structures in the velocity field. The present hotter-to-colder template is found to be the most suitable for the present analysis.

Following convergence of the temperature ensemble average, velocities and correlations were averaged at the same (τ) locations within the recorded data files where $\langle\theta^*\rangle$ was obtained. In this way, velocities in different measurement planes are conditionally sampled based upon temperature information only, and the educed average velocity and correlation patterns should correspond unambiguously to those for temperature. This technique is exactly the same as that used by Vernet *et al.* (1997) in a single plane.

The present technique resembles that applied by Antonia *et al.* (1987) in that events occurring in the temperature field are used as a trigger to identify and ensemble average events in the velocity field. Their conditional averaging technique was triggered on large values of the first time derivative of temperature occurring simultaneously at several positions spaced in a homogeneous (horizontal) plane. In addition, they required the structures to be grouped in an alternating (quasi-periodic) mode. In the present work, the PR procedure searches for the gradients via the spatial contours of the fluctuating temperature field in the homogeneous plane, specifically, hotter-to-colder transitions (see figure 2*b*). Hotter-to-colder transitions represent turbulent–non-turbulent flow transitions if hotter fluid is associated with 'older' turbulent wake flow and colder fluid with potential or more recently entrained flow. We did not add the additional criterion of alternating or symmetric modes because this limits the number of structures identified and because the separation of adjacent structures is random (see Ferré & Giralt 1989*a* and the Appendix) without significantly improving the smearing problem inherent to conditional averaging techniques.

3.3. *Smearing of ensemble averages*

One of the problems all conditional averaging procedures suffer from is that the events to be detected are individually different so that identification becomes arbitrary since a threshold is required to make decisions about whether an individual pattern belongs to the class of patterns in question. Differences in the coherent events can be of size, intensity and/or orientation, and are certainly also due to differences in the incoherent motions which accompany the coherent motions. This results in smearing when the detected structures are averaged. Smearing can be minimized by using multiple sensors and using multiple conditions in the detection procedure.

Hussain & Hayakawa (1987) point out that a single sensor cannot differentiate between a large but weak structure and a small intense structure. The use of multiple probes addresses this point. Four temperature sensors were used in the present detection procedure, each separated by $0.56l_0$. With this probe separation, it is implicitly assumed that the structures we are attempting to identify scale with the size of the half-wake. Thus, a temperature transition passing all four probes (as identified with $\gamma(\tau)$) indicates the presence of a large-scale temperature event. This could not be inferred with a single sensor.

When multiple conditions are used, some knowledge of what is being identified is required. For example, additional conditions might give explicit ranges of size, intensity or orientation so that the variation due to each of these is minimized. From a pattern recognition perspective, these additional constraints mean adding subclasses of patterns within an overall class of pattern. Such conditions are generally subjective because a threshold must be chosen. If it can be shown that the subclasses are naturally clustered, the threshold should be irrelevant (see the discussion about clustering in Ferré & Giralt 1989*a*).

In the present work the multiple condition criterion is not met because the velocity data are obtained in 72 different data files, each at a different location. Since the velocities at different locations within the structure are vastly different, we can see no rational additional condition to be placed on identification. This could be done with data obtained in a single plane by requiring that, for example, the two foci of the double roller both be present with only a small angle between the line joining the foci and the z (spanwise) coordinate direction. This cannot be done with the present data.

To investigate the effects of additional constraints, a colder-to-hotter-to-colder template is utilized, with the results described in the Appendix. As mentioned above, it is found that the spacing between adjacent coherent structures is random with the result that the ensemble averaged pattern is just the hotter spot coincident with the coherent structure described in the following sections. We have concluded that the hotter-to-colder gradient of temperature is the best choice of template in the present work.

3.4. *Temperature ensemble averages*

The ensemble average of the temperature fluctuations, $\langle\theta^*\rangle$, at $Y^* = 1.0$ corresponding to rapid hotter-to-colder temperature transitions, is shown in figure 2(b). The flow is moving from left to right in this and the following figures and the contours were interpolated and smoothed using a cubic spline function in Tecplot 7.0. On average, 592 temperature events were selected from the 72 data files. This accounts for about 42% of the recorded data. The standard deviation of the number of temperature events selected is 32, while the mean and standard deviation of $\langle\theta^*\rangle_{max}$ are 1.51 and 0.08, respectively. Thus, it can be concluded that figure 2(b) is representative of all the data files and that compiling the velocity averages from these data files is reasonable.

The temperature pattern in figure 2(b) is characterized by a progressive rise in temperature followed by a steep hotter-to-colder transition as the flow structures are advected past the probes. Vernet *et al.* (1997) also found, using a rake of temperature sensors that spanned a wider portion of the flow than for the present data, that the hotter spot (hotter than the average temperature of the fluid at this location) is surrounded by colder fluid motions in the spanwise direction. It is also observed that the temperature transition also moves slightly upstream with iteration. We have no explanation for this.

4. Topology of the prototypical coherent structure

4.1. *Velocity patterns*

Figure 3(a) shows $(\langle u^*\rangle, \langle w^*\rangle)$ in the (X^*, Z^*)-plane at $Y^* = 1$. It is clearly observed in this plot with the extended rake of 16 X-wires that a double roller configuration in the velocity field exists and that it occurs simultaneously with the hotter-to-colder transition in the temperature field (cf. figures 2b and 3a). (Note that, for clarity, only every third vector is shown.) Two foci are associated with the double roller structure in this plane. This velocity pattern is similar to that determined by Vernet *et al.* (1997) using the temperature field to identify the velocity patterns and by Giralt & Ferré (1993) and Kopp *et al.* (1997) analysing velocity data directly at $x/D = 420$. It is observed when comparing figures 2(b) and 3(a) that the hotter temperatures are located in the vicinity of the symmetry plane of the double roller and correspond to fluid with negative streamwise velocity fluctuations, or in other words, fluid motions with a deficit of momentum. Colder fluid upstream (to the left in the figures) of

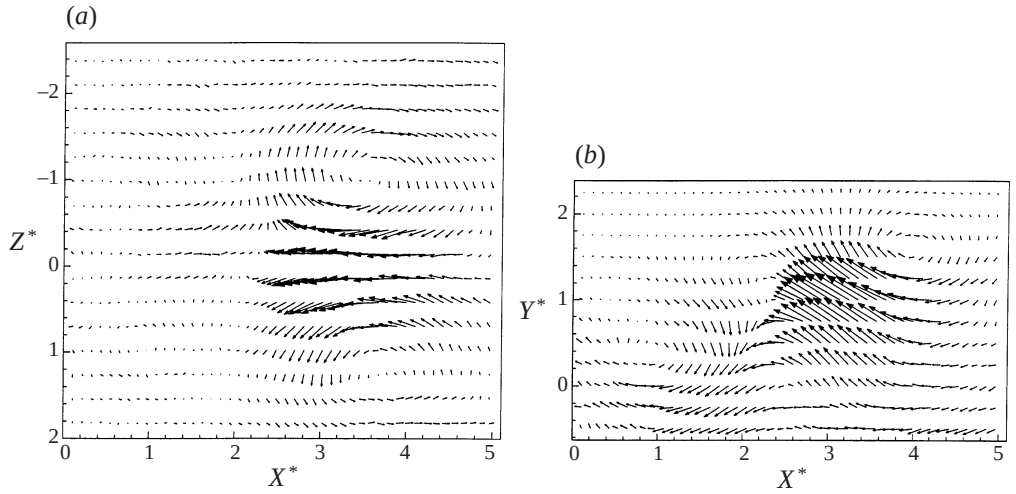

FIGURE 3. Ensemble averages of (*a*) $\langle u^* \rangle, \langle w^* \rangle$ in the (X^*, Z^*)-plane at $Y^* = 1.0$ and (*b*) $\langle u^* \rangle, \langle v^* \rangle$ in the (X^*, Y^*)-plane at $Z^* = -0.14$.

the location of the saddle point (located at $X^* = 2.4$, $Z^* = -0.14$) is associated with positive streamwise velocity fluctuations, i.e. fluid motions with an excess of momentum. Positive streamwise velocity fluctuations are also observed outside the two foci of the double rollers in the region where $Z^* < -1$ and $Z^* > 1$.

Figure 3(*b*) shows the $(\langle u^* \rangle, \langle v^* \rangle)$ projections of the velocity fluctuation vectors in the (X^*, Y^*)-plane at $Z^* = -0.14$. This figure is assembled from measurements made in the 12 different (X^*, Z^*)-planes described in § 2. Again, only results from the upper half-wake are shown because there is no regular alternating or symmetric alignment of the coherent structures in the lower half-wake relative to the structures in the upper half-wake (Vernet 1997), and vice versa. Antonia *et al.* (1987) identified structures which were in either alternating or symmetric modes. However, Vernet (1997) found that when identification is fixed on one side of the wake, coherent structures on the other side appear randomly.

Figure 3(*b*) shows that in the vertical symmetry plane of the double roller structure the $\langle u^* \rangle, \langle v^* \rangle$ velocity patterns have the same organization, a spanwise eddy, as found by Giralt & Ferré (1993) who analysed the velocity data from the vertical plane directly. The dominant feature of the average spanwise eddy in figure 3(*b*), in the centreplane of the double roller structure, is the strong outward motions with a relatively weak-looking circulation pattern centred at $x^* = 4.0$ and $y^* = 1.6$. These motions must be Grant's mixing jets (Vernet *et al.* 1997). The circulation pattern, which has spanwise vorticity, is much weaker than that observed by Antonia *et al.* (1987) due to the fact that a triple decomposition is used here (see the discussion in Giralt & Ferré 1993, as well).

Since the velocity data are assembled from 72 separate data files it is difficult to determine with the present data whether the double roller configuration is a real instantaneous flow structure. This issue has been investigated by Ferre-Gine *et al.* (1997) who found that the double roller vortex configuration is a real instantaneous flow structure most of the time and is not just an artifact of the averaging procedure. However, the strengths of the individual foci are often not equal, with one side being much stronger than the other. Therefore, the observed symmetry comes about from

averaging a large number of these structures. Additionally, they found that the line joining the two foci making up the double roller may not be parallel to the spanwise axis instantaneously. Again, the averaging process causes the symmetry although it is emphasized that the instantaneous flow structures are similar, i.e. belong to the same class. These instantaneous differences cause smearing of the ensemble averages, as discussed in § 3.2.

In both figures 3(*a*) and 3(*b*) a saddle point is visible at roughly the same lateral location as that observed by Antonia *et al.* (1987). Figure 3 of Bisset *et al.* (1990) shows how these critical points can occur instantaneously in the velocity field. In the remainder of the paper, when the saddle point is mentioned, the coordinate location ($X^* = 2.4$, $Y^* = 1.0$, $Z^* = -0.14$) is intended. The existence of this saddle point upstream of the structure surprised us initially because we expected that it was an 'artifact' of the periodic organization specifically identified by Antonia *et al.* However, the vertical plane (figure 3*b*) also contains an upstream vortex structure centred at approximately $X^* = 1$. This second upstream vortex structure is badly smeared. Ferré & Giralt (1989) did an extensive analysis of the structure spacing and found that there was little evidence for highly repetitive groupings of structures and this upstream vortex is likely due to the occasional alignment of an upstream vortex. It seems probable that any given upstream structure, relative to the identified ones, will be randomly situated in both the streamwise and spanwise directions. The saddle point and this upstream vortex are further discussed in § 4.3 since a discussion of critical points is best done in the context of streamline patterns.

4.2. *Spatially averaged coherent velocities*

For coherent structures to be dynamically significant they should contribute to the mean velocity field even when a triple decomposition is assumed and the local mean velocity is removed from the analysis of the structures. In this subsection, the coherent contribution to the mean field is investigated by examining spatial averages of the coherent motions. If the coherent streamwise velocity, $u_c(x, y, z)$, defined by equation (3), is averaged over the streamwise coordinate, x, we obtain $\overline{U}_c(y, z) = \overline{u_c(x, y, z)}$ where the overbar indicates the spatial average. If $\overline{U}_c(y, z)$ is then averaged over the spanwise coordinate, z, we obtain $\overline{\overline{U}}_c(y)$. Plots of $\overline{U}_c(y, z)$ are shown in figure 4(*a–d*) and $\overline{\overline{U}}_c(y)$ in figure 4(*e*). Here $\overline{U}_c(y, z)$ has been normalized by u'_0, the streamwise r.m.s. velocity at $Y^* = 1$.

Figure 4(*a–d*) shows the spanwise variation of the mean velocity profile due to the coherent motions. Between the two foci in the horizontal plane in the region bound by approximately $-1.2 < Z^* < 1.2$ at $Y^* = 1$ there is a distinct velocity defect due primarily to the negative streamwise velocity fluctuations of the mixing jet region. The magnitude of the peak defect is largest near the symmetry plane of the coherent structure and is found to be less than u'_0. Outside the two foci, where $Z^* < -1.2$ and $Z^* > 1.2$, $\overline{U}_c(y, z)$ is positive so that there is a mean velocity excess, but of smaller magnitude than the maximum defect. Clearly, the coherent velocities make a significant contribution to the mean velocity field instantaneously even though we are applying a triple decomposition and the 'true' mean velocity was removed prior to analysis.

Libby (1976) found that the velocity field within the turbulent bulges in wakes has less momentum than the mean while the potential regions have greater than average momentum. The present results are consistent with bulges located in the region with a momentum deficit bounded by approximately $-1.2 < Z^* < 1.2$ at $Y^* = 1$, while

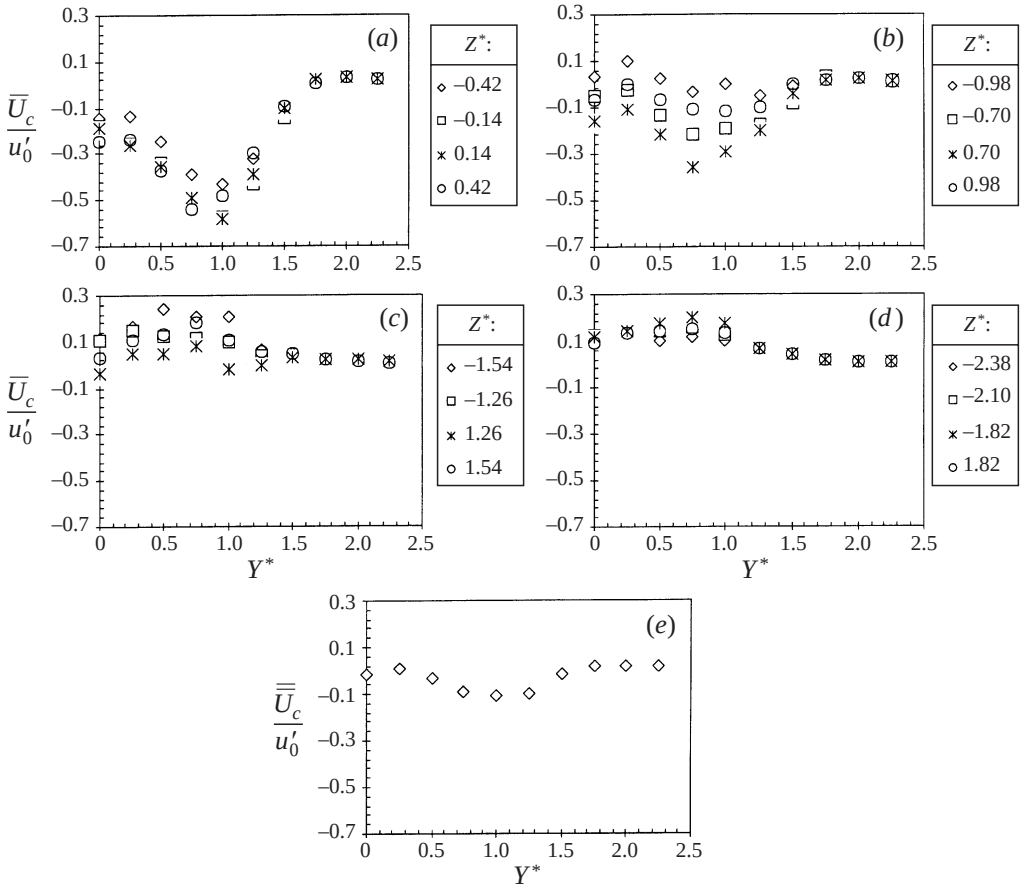

FIGURE 4. (*a–d*) Profiles of $\overline{U}_c(y,z)$ at all the z^*-locations and (*e*) the $\overline{\overline{U}}_c(y)$ profile.

the outer edges of the structure with excess of momentum, in the region $Z^* < -1.2$ and $Z^* > 1.2$, are consistent with the potential regions surrounding adjacent bulges.

When $\overline{U}_c(y,z)$ is averaged over the spanwise coordinate, z, to remove the spanwise dependence and to obtain $\overline{\overline{U}}_c(y)$ one would expect $\overline{\overline{U}}_c(y)$ to be near zero since approximately one-third of the flow has gone into the average and this is an analysis of the fluctuations from the local time mean. Interestingly, there is a small defect remaining, as observed in figure 4(*e*), which could be due to not including data upstream of the saddle point where there are primarily positive streamwise velocity fluctuations, to numerical errors in the integration over the spanwise coordinate, and/or to smearing. Since the coherent structures occur randomly in the spanwise direction in the far-wake region, the (total) mean velocity in plane wakes is, at any particular streamwise location, dependent only on the lateral coordinate, y.

4.3. *Streamline patterns and critical points*

Critical points are locations where streamlines are indeterminate and velocities vanish. Chong, Perry & Cantwell (1990) have classified the topology of three-dimensional critical points. Figure 5 depicts sectional streamline patterns obtained from the vectors $(\langle u^* \rangle + U^* - U_{conv}, \langle v^* \rangle)$ and $(\langle u^* \rangle + U^* - U_{conv}, \langle w^* \rangle)$, where $U_{conv} = 0.95U_0$. These streamlines were calculated with a built-in feature in Tecplot 7.0. Sectional streamlines

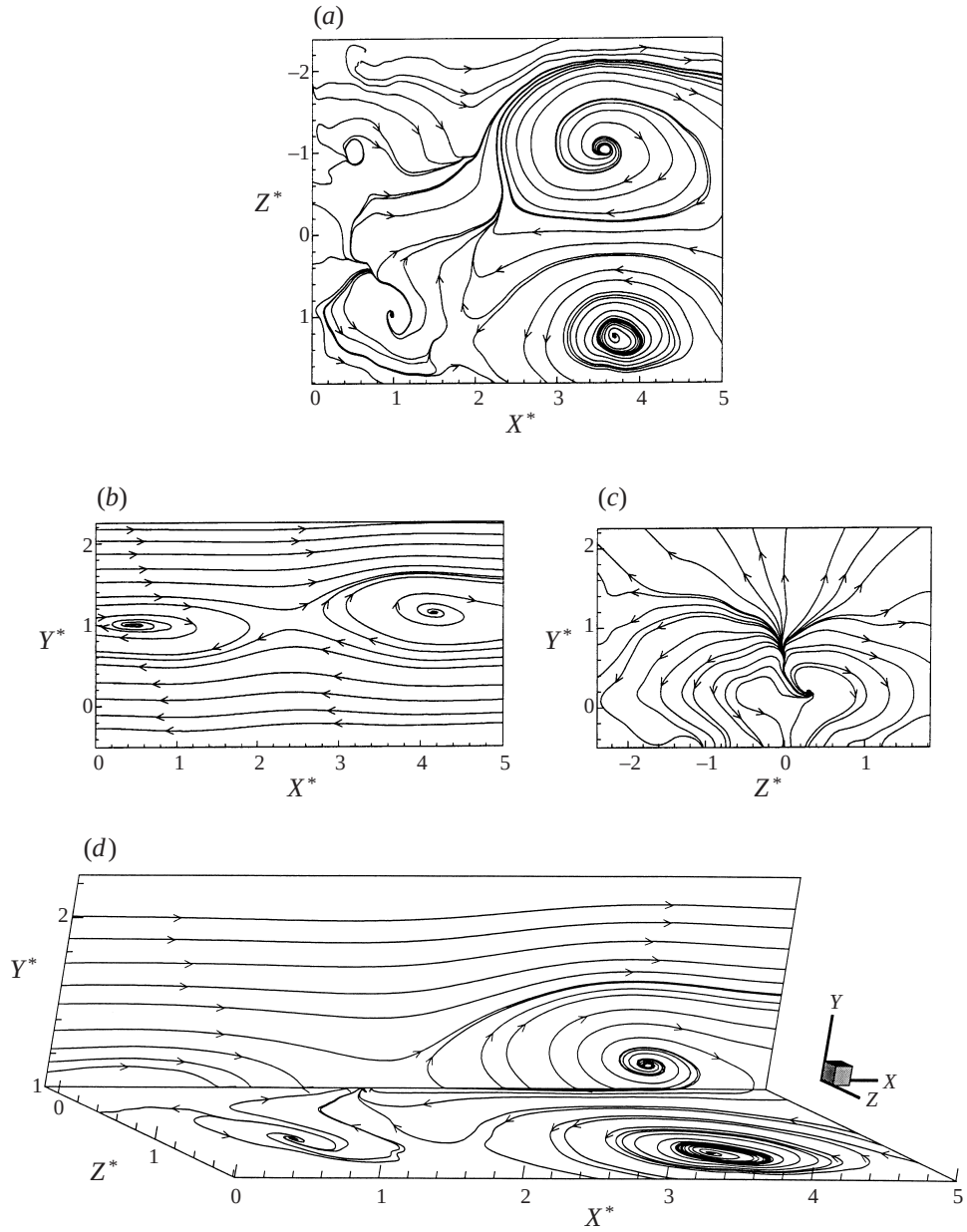

FIGURE 5. Sectional streamline patterns of (*a*) ($\langle u^* \rangle + \overline{U} - U_{conv}$, $\langle w^* \rangle$) in the (X^*, Z^*)-plane at $Y^* = 1.0$, (*b*) ($\langle u^* \rangle + \overline{U} - U_{conv}, \langle v^* \rangle$) in the (X^*, Y^*)-plane at $Z^* = -0.14$, (*c*) ($\langle v^* \rangle, \langle w^* \rangle$) in the (Y^*, Z^*)-plane at $X^* = 2.5$, and (*d*) a three-dimensional view of the sectional streamlines.

clearly show the foci and the saddle point in both the vertical and horizontal planes. Figure 5(*a*) shows the sectional streamlines in the horizontal plane at $Y^* = 1$, figure 5(*b*) shows the vertical symmetry plane at $Z^* = -0.14$ and figure 5(*c*) shows the (Y^*, Z^*)-plane at $X^* = 2.5$. Figure 5(*d*) shows these sectional streamlines in a three-dimensional view.

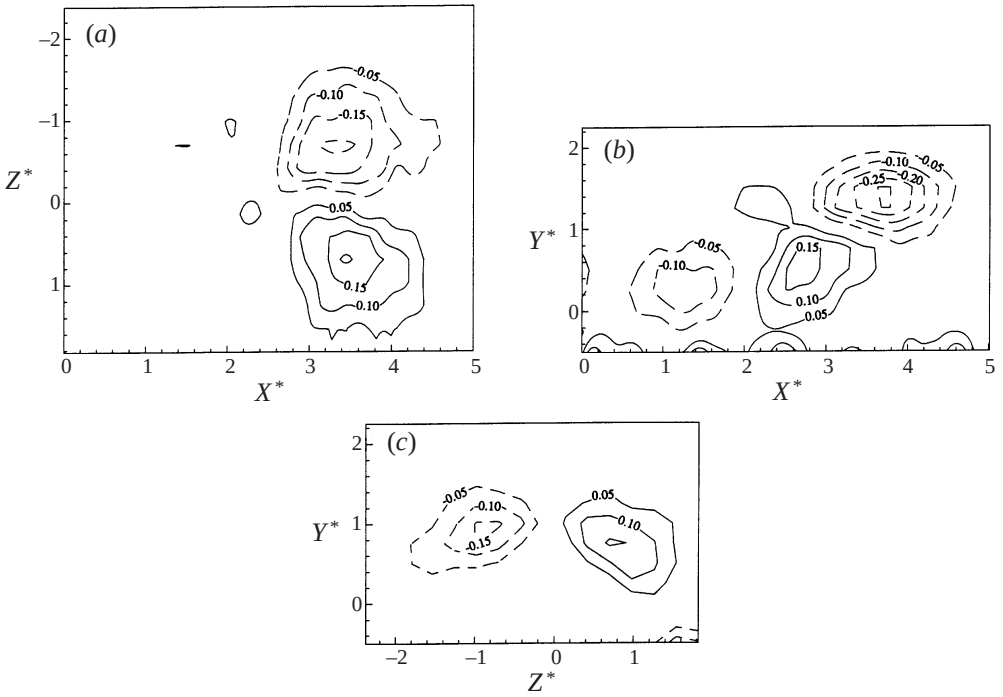

FIGURE 6. Ensemble average of (*a*) $\langle \omega_y \rangle$ in the (X^*, Z^*)-plane at $Y^* = 1.0$, (*b*) $\langle \omega_z \rangle$ in the (X^*, Y^*)-plane at $Z^* = -0.14$, (*c*) $\langle \omega_x \rangle$ in the (Y^*, Z^*)-plane at $X^* = 3.5$.

Several critical points can be observed, as discussed in §4.1. There are two foci associated with the double roller motions in the horizontal plane centred at approximately $X^* = 3.5$ and $Z^* = \pm 1.1$, two foci in the vertical plane at about $Y^* = 1$ and $X^* = 0.5$ and 4.2, and the saddle point at ($X^* = 2.4$, $Y^* = 1.0$, $Z^* = -0.14$). Figure 5(*c*) is a slice of the saddle point in the (Y^*, Z^*)-plane. All of the critical points are observed to be unstable (Kaplan 1958) because the fluid is flowing away from them.

The saddle point upstream of the main structure appears to be distorted in the horizontal plane (see figure 5*a*). This is probably due to some misalignments in the ensemble averaging because not all of the individual saddle points are perfectly aligned with the centre of the hotter-to-colder temperature transition. As a result, continuity is not well satisfied in this region, as discussed in §4.4. It seems likely that saddle points would be more susceptible to smearing than foci due to their highly three-dimensional nature (as compared to foci, for example).

The results shown in figure 5(*b*) can be compared with those of Bisset *et al.* (1990) noting the difference in the detection schemes applied. These authors identify structures in either alternating or symmetric modes while in the present work we identify structures on only a single side of the wake. Thus, for comparison purposes only a single side of their results should be examined. Our results are similar to their symmetric mode structures (in their figures 6 and 7). In fact, their '*v*-detection' scheme applied to symmetric mode structures is not unlike our technique in that they identify the saddle point between two adjacent structures. Similarly, we identify a temperature transition which happens to be the location of this same saddle point. Keeping in mind that their flow is from right to left, it is interesting to note that the focus upstream of the saddle point is slightly closer towards the centreline, as can be observed in our figure 5(*b*).

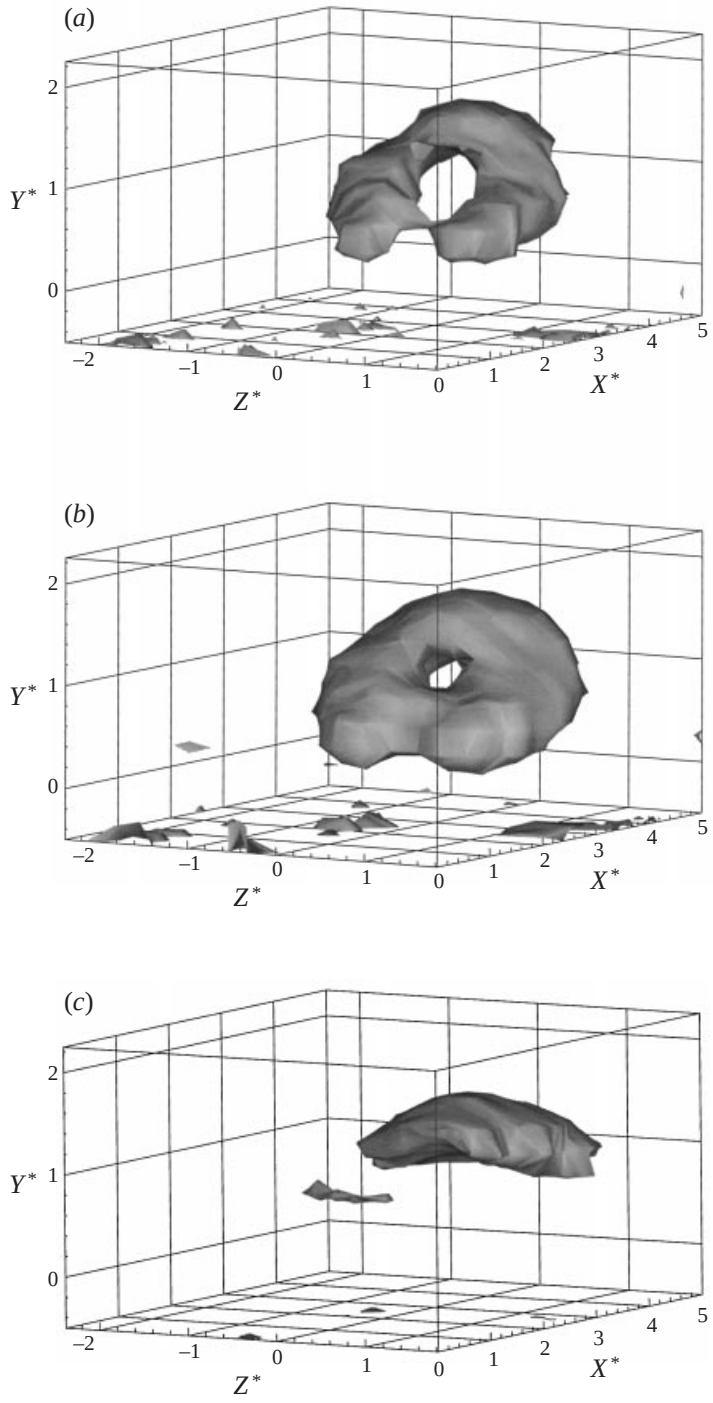

FIGURE 7. Three-dimensional view of vorticity iso-surfaces (*a*) $|\omega| = 0.6|\omega|_{max}$, (*b*) $|\omega| = 0.5|\omega|_{max}$ and (*c*) $|\omega + \Omega| = 0.75|\omega + \Omega|_{max}$.

The question is open as to whether the saddle point exists because of the presence of two adjacent vortices (separated in the streamwise direction) or whether it is a feature associated with the hotter-to-colder transition regardless of the spacing between adjacent vortices. On balance, it seems to us that the saddle point exists regardless of the spacing, given the strength of the inward and outward velocity fluctuations in its immediate vicinity. Specifically, the outward fluctuations of the upstream vortex near $X^* = 0$ are weak compared to those within the main structure at $X^* = 3$. The inward velocities just upstream of the saddle ($X^* = 2$) are much stronger than those associated with the main vortex structure near $X^* = 5$. Kopp *et al.*'s (1995) kinematic vortex model of this type of structure shows that the inward velocities are weaker than the outward lateral velocities due to the shape of the structure. For this reason, it seems likely that the saddle point exists regardless of the spacing between adjacent vortices.

Bisset *et al.* (1990) developed a kinematic model of the far wake using an array of Rankine vortices with streamwise velocities having a phase difference from the lateral velocities. With this phase difference, double roller patterns are observed in horizontal planes at $Y^* = 1$. There are, however, significant differences in these patterns and our prototypical coherent structure. The main difference is observed at the location of the vortex centres in the vertical, (X^*, Y^*)-plane. In their model, the vortex centres in the (X^*, Y^*)-plane occur simultaneously with saddle points in the horizontal, (X^*, Z^*)-plane at $Y^* = 1$ (see their figure 15). In contrast, our experimental/pattern-recognition results indicate only a deficit of streamwise momentum. Thus, their model double rollers are half the streamwise scale of ours.

4.4. *Continuity*

The coherent velocity field should satisfy continuity,

$$\frac{\partial \langle u^* \rangle}{\partial X^*} + \frac{\partial \langle v^* \rangle}{\partial Y^*} + \frac{\partial \langle w^* \rangle}{\partial Z^*} = 0. \tag{8}$$

The divergence of the present velocity data shows that the largest absolute value of the sum of the left-hand side of equation (8) is 0.18 and occurs near the saddle point because the spatial configuration of this critical point is not 'perfect'. The peak value is of the order of the largest derivative observed in the coherent field. The mean value is 0.0005. Generally, isocontours of the left-hand side of equation (8) are randomly distributed. The one exception to this is in the region immediately downstream of the saddle point where the error is relatively large over a region covering approximately $0.2l_0$ in the X^*- and Y^*-directions, but l_0 in the Z^*-direction. This error can be inferred from figure 5 by examining the streamlines in the immediate vicinity of the saddle point and realizing the large velocity gradients that occur in this region. In general, the deviations from equation (8) obtained with the present data support the conclusion that the measured coherent velocity field satisfies continuity.

4.5. *Vorticity patterns*

Figure 6 depicts contours of the coherent lateral, spanwise and streamwise vorticity fluctuations, which are, respectively,

$$\left.\begin{aligned} \langle \omega_y \rangle &= (\partial \langle u^* \rangle / \partial Z^* - \partial \langle w^* \rangle / \partial X^*), \\ \langle \omega_z \rangle &= (\partial \langle v^* \rangle / \partial X^* - \partial \langle u^* \rangle / \partial Y^*), \\ \langle \omega_x \rangle &= (\partial \langle w^* \rangle / \partial Y^* - \partial \langle v^* \rangle / \partial Z^*). \end{aligned}\right\} \tag{9}$$

Figure 6(*a*) depicts the lateral vorticity at $Y^* = 1.0$ while figure 6(*c*) shows the streamwise vorticity at $X^* = 3.5$. Both figures show two lobes which, together with the spanwise vorticity distribution in figure 6(*b*), is consistent with an inclined double roller structure. The vorticity magnitude is not quite equal in each lobe. Figure 6(*b*) shows that there are four lobes associated with the spanwise vorticity in the vertical symmetry plane. The highest levels occur downstream of the saddle point and, from the location of the maxima, it is observed that the focus of the spanwise eddy (i.e. the focus in the vertical centreplane of the structure) is located at (3.6, 1.4, −0.14). There are also closed contours of spanwise vorticity upstream of the saddle point due to the adjacent upstream vortex described earlier.

The spanwise vorticity, depicted in figure 6(*b*), is quite different to that reported by Antonia *et al.* (1987) because mean vorticity is not included in this plot. The mean vorticity in a plane wake has only a spanwise component,

$$\Omega_z = \frac{\partial V^*}{\partial X^*} - \frac{\partial U^*}{\partial Y^*} \sim -\frac{\partial U^*}{\partial Y^*}. \tag{10}$$

Three-dimensional plots of $|\omega|$ isocontours are shown in figures 7(*a*, *b*) while $|\omega + \Omega|$ is shown in figure 7(*c*) where $|\omega| = (\omega_x^2 + \omega_y^2 + \omega_z^2)^{1/2}$ and $|\omega + \Omega| = (\omega_x^2 + \omega_y^2 + (\omega_z + \Omega_z)^2)^{1/2}$. Figure 7(*a–c*) shows three very different 'vortices', namely a horseshoe, a vortex ring and a tube. These depend strongly on the iso-level shown.

Since the vorticity of the mean velocity is negative in the upper half of the wake, adding the mean vorticity enhances the main lobe of the structure and reduces the lobes with positive $\langle\omega_z\rangle$. The lateral and streamwise vorticity are also smaller relative to $\langle\omega_z\rangle + \Omega_z$ so that the vorticity iso-surface in figure 7(*c*) is less three-dimensional and is more like a tube.

Clearly the mean flow changes the 'appearance' of the coherent till here structure as does the iso-level of the vorticity magnitude. The difference between the $|\omega| = 0.5|\omega|_{max}$ and $|\omega| = 0.6|\omega|_{max}$ iso-surfaces in figure 7(*a*, *b*) is substantial: one is a vortex ring and the other a horseshoe. Lower iso-surface levels do not show the structure clearly as $|\omega|$ tends to fill the plot as the plotted contours approach zero. A more detailed analysis regarding whether or not this coherent structure is a vortex, and what its shape is, is contained in the next section.

5. Is the coherent structure a horseshoe vortex?

5.1. *Definition of a vortex in turbulent shear flows*

There has been much debate in the literature about what constitutes a vortex in turbulent shear flows (see Chong *et al.* 1990; Jeong & Hussain 1995). Although this problem may be somewhat academic, it is nevertheless interesting, especially since coherent structures are now commonly viewed as vortices. The essential difficulty of defining a vortex is identifying its boundaries when it is placed in a strain field. There are problems with using vorticity iso-surfaces to visualize the boundaries of vortices since vorticity is not an invariant and a threshold is needed to identify the boundaries. In regions with high rates of strain, the threshold also needs to be very high, perhaps hiding features of the vortex itself. Boundaries identified in this way are then somewhat arbitrary as discussed in § 4.5 and illustrated in figure 7(*a–c*).

Various definitions of functions which demarcate vortices have been developed to overcome this deficiency, such as those by Hunt, Wray & Moin (1988) and Jeong & Hussain (1995). The definition of Hunt *et al.* is that an 'eddy' is a region with a

positive second invariant of the velocity gradient tensor, $\partial u_i/\partial x_j$, and with a pressure minimum. Jeong & Hussain point out that there is no explicit connection between regions with a positive second invariant and a pressure minimum.

In contrast, Jeong & Hussain (1995) define a vortex as the region where the second eigenvector, $\boldsymbol{\lambda}_2$, of $[\boldsymbol{S}^2 + \boldsymbol{\Omega}^2]$ is negative, where

$$S_{ij} = \tfrac{1}{2}\left(u_{i,j} + u_{j,i}\right) = \frac{1}{2}\left(\frac{\partial u_i}{\partial x_j} + \frac{\partial u_j}{\partial x_i}\right) = \frac{1}{2}\left(\frac{\partial u^*_{ci}}{\partial X^*_j} + \frac{\partial u^*_{cj}}{\partial X^*_i} + \frac{\partial U^*_i}{\partial X^*_j} + \frac{\partial U^*_j}{\partial X^*_j}\right), \tag{11}$$

$$\Omega_{ij} = \tfrac{1}{2}\left(u_{i,j} - u_{j,i}\right) = \frac{1}{2}\left(\frac{\partial u_i}{\partial x_j} - \frac{\partial u_j}{\partial x_i}\right) = \frac{1}{2}\left(\frac{\partial u^*_{ci}}{\partial X^*_j} - \frac{\partial u^*_{cj}}{\partial X^*_i} + \frac{\partial U^*_i}{\partial X^*_j} - \frac{\partial U^*_j}{\partial X^*_i}\right), \tag{12}$$

and $\{\boldsymbol{u}_i\} = \{U^* + \langle u^*\rangle, V^* + \langle v^*\rangle, \langle w^*\rangle\}$. The boundary of the vortex would be the iso-surface where $\boldsymbol{\lambda}_2 = 0$.

The mean shear in the far wake, $\partial U^*/\partial Y^*$, presents some additional difficulties in terms of understanding its physical significance as related to coherent structures. On the one hand, researchers have separated the mean velocity and the turbulent fluctuations in fully developed flows to evaluate theories such as self-preservation. Based on this decomposition, Townsend's (1956) and Grant's (1958) 'big eddies' and double rollers were inferred from correlation measurements. Payne & Lumley's (1967) proper orthogonal decomposition, which is based on finding the motions which maximize the contribution to the turbulence energy, identified a similar structure. Such structures must be in dynamic equilibrium for self-preservation to exist. In addition, there is experimental (e.g. Wygnanski *et al.* 1986) and DNS (Moser, Rogers & Ewing 1998) evidence which shows that the shape of the mean velocity profile in far wakes is universal although there can be significant differences in the velocity and length scales which normalize it. Experiments and DNS have also shown that the structure of the fluctuations depends strongly on the initial conditions (e.g. Kopp & Keffer 1996; Moser *et al.* 1998). This raises the interesting question as to whether far-wake structures can alter mean velocity profiles by their presence. Since the profile shape is universal, it would appear that their role could only be to adjust the magnitude of the normalizing length and velocity scales.

On the other hand, coherent structures are known to have convection velocities, that is, they move in a 'coherent' manner which can be tracked visually. In this case, some portion (if not all) of the mean shear must be directly associated with the coherent structures. This makes a lot of sense in near wakes where one can intuitively see that the Kármán vortices should contribute to the mean flow because their vorticity is aligned with that of the mean flow. It is also interesting to note that Bisset *et al.* (1990) developed a kinematic far-wake model based on an array of vortices which successfully represented the mean defect profile (although it did not get the three-dimensional structure quite right – see § 4.1). Thus, a strong argument can be put forward that some of the mean shear must be associated with the coherent structure. In addition, if the structure were convected at the local mean velocity it would be elongated very rapidly and would not be 'self-similar'. However, similar structures have been observed in experimental data from different facilities in cylinder wakes from approximately $x/D \sim 80$ to 400. Therefore, it seems highly probable that the structures must be convected at some convection velocity other than the local mean.

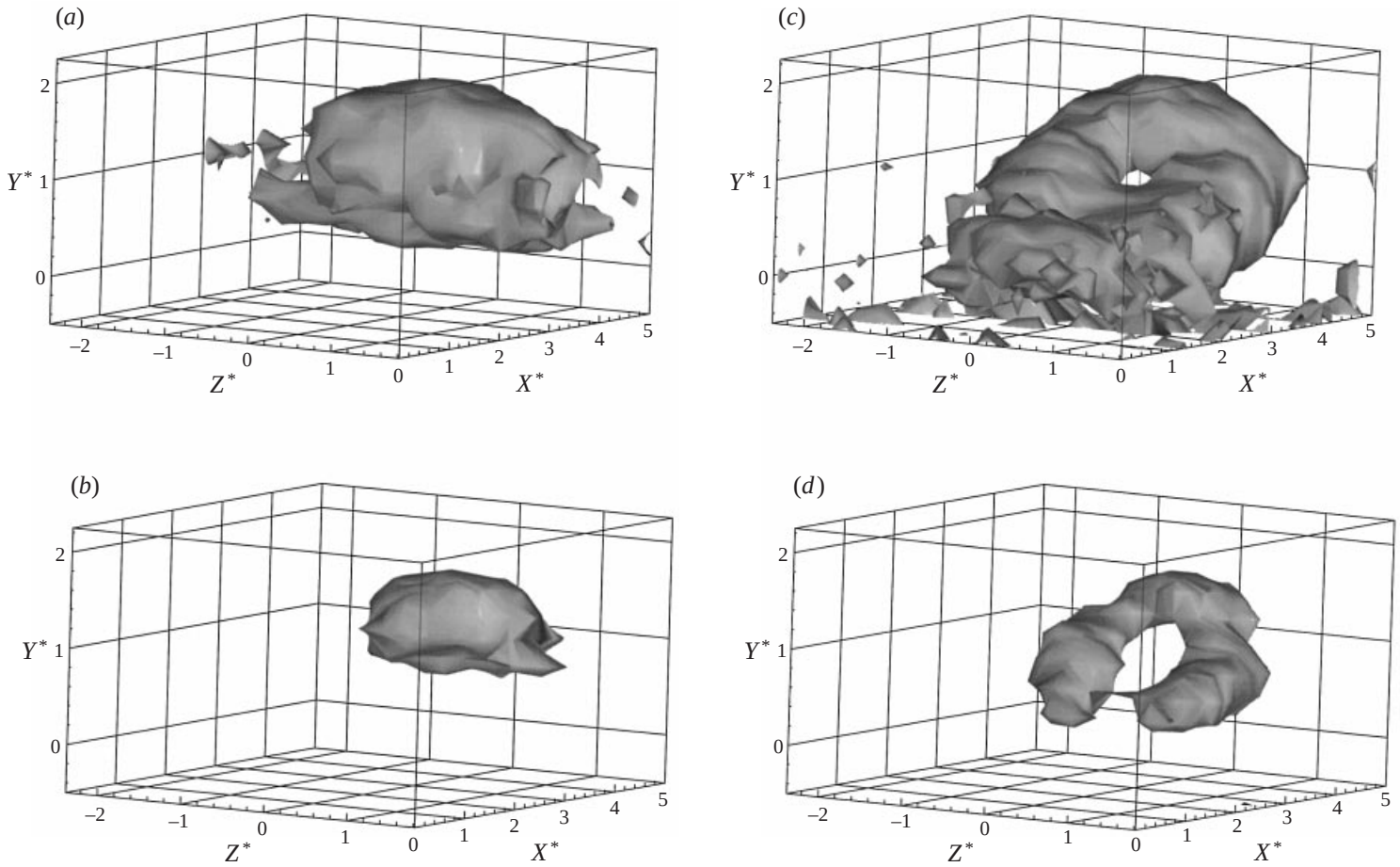

FIGURE 8. Three-dimensional view of λ_2 associated with the coherent structure when the mean and coherent velocity fields are considered with iso-surfaces of (*a*) 5% and (*b*) 30% of $|\lambda_2|_{max}$; and when only the coherent velocity field is considered with iso-surfaces of (*c*) 5% and (*d*) 30% of $|\lambda_2|_{max}$.

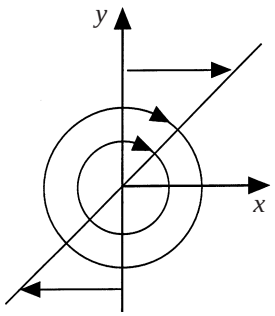

FIGURE 9. Sketch of a Rankine vortex in a uniform mean shear.

5.2. *The shape of the vortex*

Figure 8 shows three-dimensional isocontours of λ_2 for two different cases, namely, when the mean shear is considered and when it is ignored. When the mean shear is included, the λ_2 contours should approximate the shape of the actual vortex in the flow. When it is neglected and a triple decomposition is used, the λ_2 contours can be viewed as the 'vortex structure of the fluctuations'. Figure 8(*a*) shows the contours of λ_2 equal to 5% of $(-\lambda_2)_{max}$ while figure 8(*b*) shows the contours when λ_2 is equal to 30% of $(-\lambda_2)_{max}$ with the mean gradients included in the analysis. Here, the terms involving $\partial V^*/\partial X^*$, $\partial V^*/\partial Y^*$ and $\partial U^*/\partial X^*$ are approximated using continuity and $U_s \propto x^{-1/2}$, with only $\partial U^*/\partial Y^*$ determined experimentally. Obviously, the magnitudes of $\partial V^*/\partial X^*$, $\partial V^*/\partial Y^*$ and $\partial U^*/\partial X^*$ are much smaller than $\partial U^*/\partial Y^*$ in the far wake. In both figures 8(*a*) and 8(*b*) the vortex has the shape of a tube. This tube roughly spans the distance between the two foci in the spanwise direction ($-1 < Z^* < 1$ at $Y^* = 1$), and in the streamwise direction between $X^* = 2.4$ and $X^* = 5$. The saddle point is not part of the vortex.

Figure 8(*c*, *d*) shows λ_2 when only the coherent velocity field is considered. In this case the 5% contour level is shaped like a ring (figure 8*c*) while the 30% contour level is a horseshoe (figure 8*d*). One can easily see that the upstream limit of the ring is the saddle point. The mixing jet region is partially within and partially outside the vortex boundary. The whole vortex is clearly shear aligned. Plots of the positive iso-surfaces of the second invariant, not shown here, also reveal the same topology.

The above results show that the mean shear affects the eigenvectors. This makes sense. In a fully developed plane wake, $\lambda_2 \geqslant 0$ everywhere when only the mean shear is analysed. Thus, one would expect the mean shear to affect the eigenvalues of $[\boldsymbol{S}^2 + \boldsymbol{\Omega}^2]$, especially in the region where the mean shear is largest, i.e. near $Y^* = 1.0$. Increasing the mean shear also increases the absolute value of $(-\lambda_2)_{max}$. Because the mean rate of strain is relatively large in the far wake, its inclusion in the analysis causes the 'shape' of the vortex and the 'structure of the fluctuations' to be rather different.

One of the issues that needs clarification is whether all of the mean shear should be accounted for by the coherent structures in the far wake or whether some 'pure' shear remains. It should be noted that if not all the mean shear is included with the coherent structure, then the vortex boundary becomes arbitrary, as shown with the simple example below. If one considers a Rankine vortex placed in the (x, y)-plane with a pure shear defined by the mean velocity field $\overline{U} = Sy$, as shown in figure 9,

where

$$u = \begin{cases} -\frac{1}{2}\omega_0 y + Sy, & r < a \\ \frac{1}{2}\omega_0 a^2 \dfrac{y}{(x^2+y^2)} + Sy, & r > a, \end{cases} \tag{13}$$

$$v = \begin{cases} +\frac{1}{2}\omega_0 x, & r < a \\ +\frac{1}{2}\omega_0 a^2 \dfrac{x}{(x^2+y^2)}, & r > a. \end{cases} \tag{14}$$

Here, the Rankine vortex has been decomposed into Cartesian coordinates with $r = \sqrt{x^2+y^2}$, $\omega_0 < 0$, and $S > 0$ as sketched. Then,

$$[\boldsymbol{S}^2 + \boldsymbol{\Omega}^2] = \begin{bmatrix} m & 0 & 0 \\ 0 & m & 0 \\ 0 & 0 & 0 \end{bmatrix}, \tag{15}$$

so that $\lambda_1 = 0$ and

$$\begin{aligned} m = \lambda_2 = \lambda_3 &= \left(\frac{\partial u}{\partial x}\right)^2 + \left(\frac{\partial v}{\partial x}\right)\left(\frac{\partial u}{\partial y}\right) \\ &= \begin{cases} -\frac{1}{4}\omega_0^2 + \frac{1}{2}\omega_0 S, & r < a \\ \dfrac{\omega_0 a^2}{(x^2+y^2)}\left[\dfrac{\omega_0 a^2}{4(x^2+y^2)} - \dfrac{Sx^2}{(x^2+y^2)} + \frac{1}{2}S\right], & r > a. \end{cases} \end{aligned} \tag{16}$$

When $r < a$, there are two negative eigenvalues ($\lambda_2 = \lambda_3 < 0$). When $r > a$ and $S = 0$, there are no negative eigenvalues since $\lambda_2 = \lambda_3 > 0$. However, it is possible to have two negative eigenvectors when $r > a$. Therefore, in the presence of mean shear, the boundary of the Rankine vortex, as visualized by λ_2, can be different from the case with no extra shear present. For the configuration shown in figure 9 (which is similar to, although not precisely the same, as the upper half plane of a wake), $\lambda_2 < 0$ when

$$\left| S\omega_0 \left(\frac{1}{2} - \frac{x^2}{(x^2+y^2)}\right)\right| > \frac{\omega_0^2 a^2}{4(x^2+y^2)} \quad \text{and} \quad \frac{1}{2} > \frac{x^2}{(x^2+y^2)}. \tag{17}$$

For example, let $(x, y) = (0, \pm 2a)$. If there is no extra mean shear ($S = 0$), then this point is not within the vortex core because the boundary is $r = a$. However, if $S > \omega_0/8$, the point $(0, 2a)$ is now part of the boundary of the vortex. Therefore, it takes relatively little shear to significantly alter the vortex boundary.

How does this relate to the coherent structure identified in this paper? Consider the vertical symmetry plane of the coherent structure where the gradients $\partial/\partial z = 0$ and $w_c = 0$. In this case, $[\boldsymbol{S}^2 + \boldsymbol{\Omega}^2]$ is described by equation (15). Clearly, $\partial U^*/\partial Y^*$ is not equal to a constant over the range $0 < Y^* < 2$. However, it is maximum near $Y^* = 1$. Our conclusion here is simply that if some significant amount of $\partial U^*/\partial Y^*$ is not accounted for by the coherent motions, the vortex boundary is arbitrary. At present, there does not appear to be any rational way of splitting the mean shear between that accounted for by the average passage of the coherent structures and that by pure shear. Note that at the outer regions of the wake ($Y^* = 2$) and near the centreline ($Y^* = 0$) the boundaries of the vortex, if they are located there, are not affected because $\partial U^*/\partial Y^* \approx 0$.

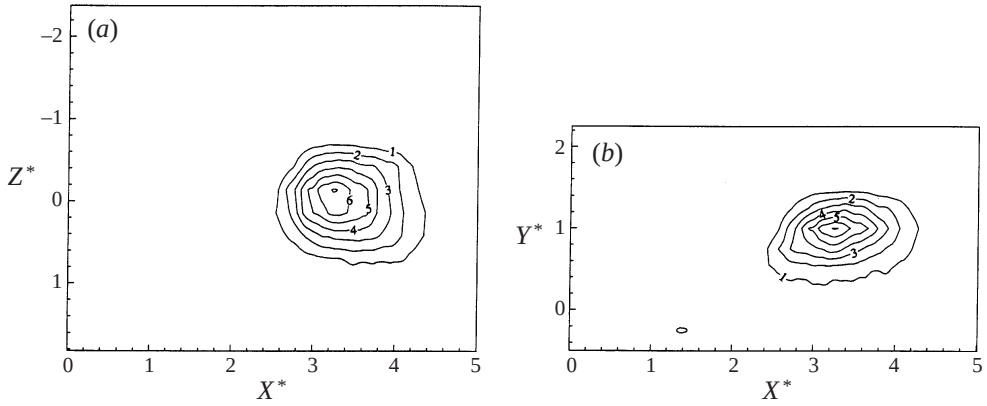

FIGURE 10. Ensemble average of $\langle u^* \rangle^2 \times 100$ in (*a*) the (X^*, Z^*)-plane at $Y^* = 1.0$ and (*b*) the (X^*, Y^*)-plane at $Z^* = -0.14$.

6. Momentum and energy transfer processes and entrainment

6.1. *Large-scale (coherent) stresses*

Figure 10 shows slices of the coherent streamwise normal stress $\langle u^* \rangle^2$ in the (X^*, Z^*)- and (X^*, Y^*)-planes, respectively. The coherent lateral normal stress $\langle v^* \rangle^2$ and coherent shear stress $\langle u^* \rangle \langle v^* \rangle$, not shown in this paper, exhibit similar behaviour. The behaviour of the spanwise normal stress, $\langle w^* \rangle^2$, which is significantly different, is discussed by Vernet (1997). Clearly, $\langle u^* \rangle^2$ is three-dimensional with a significant magnitude over a spatial extent of l_0 in the spanwise and lateral directions. The streamwise extent of $1.5l_0$ is slightly larger. The region with high $\langle u^* \rangle^2$ is centred in the symmetry plane of the coherent structure at (3.2, 1.0, 0), between the saddle point and the foci, or in other words, within the mixing jet region of the structure.

The coherent, $\langle k^* \rangle^2$, and incoherent, $\langle k_r^{*2} \rangle$, turbulence kinetic energy

$$\langle k^* \rangle^2 = \tfrac{1}{2}(\langle u^* \rangle^2 + \langle v^* \rangle^2 + \langle w^* \rangle^2), \tag{18}$$

$$\langle k_r^{*2} \rangle = \tfrac{1}{2}(\langle u^{*2} \rangle + \langle v^{*2} \rangle + \langle w^{*2} \rangle) - \langle k^* \rangle^2, \tag{19}$$

are shown in figure 11. Figure 11(*a*, *b*) shows that the spatial distribution of coherent energy is similar to the $\langle u^* \rangle^2$ isocontours given in figure 10. The incoherent turbulence kinetic energy, $\langle k_r^{*2} \rangle$, is also maximum in the mixing jet region, as shown in figure 11(*c*, *d*). The peak value of the total kinetic energy is twice that of the coherent value. Clearly, there is a lot of variation in the individual structures (or events) as evidenced by the high levels of incoherent turbulence, especially in the mixing jet region. This is examined further below, but also explains why these structures are generally difficult to identify.

6.2. *Stresses due to the incoherent (small-scale) motions*

Figure 12 shows the contours of the streamwise normal stress due to the small-scale or incoherent motions, $\langle u_r^{*2} \rangle$, calculated from $\langle u^{*2} \rangle - \langle u^* \rangle^2$, in the (X^*, Z^*)- and (X^*, Y^*)-planes. This figure shows that there is a deficit of incoherent energy in the region around the saddle point and just upstream of it at approximately (2.4, 1.0, 0). Thus, colder fluid is less turbulent, as expected. Peak values of $\langle u_r^{*2} \rangle$ are observed in the mixing jet region downstream of the saddle point. Figure 12(*b*) shows that the contours for $\langle u_r^{*2} \rangle$ in the vertical symmetry plane of the structure are similar to those

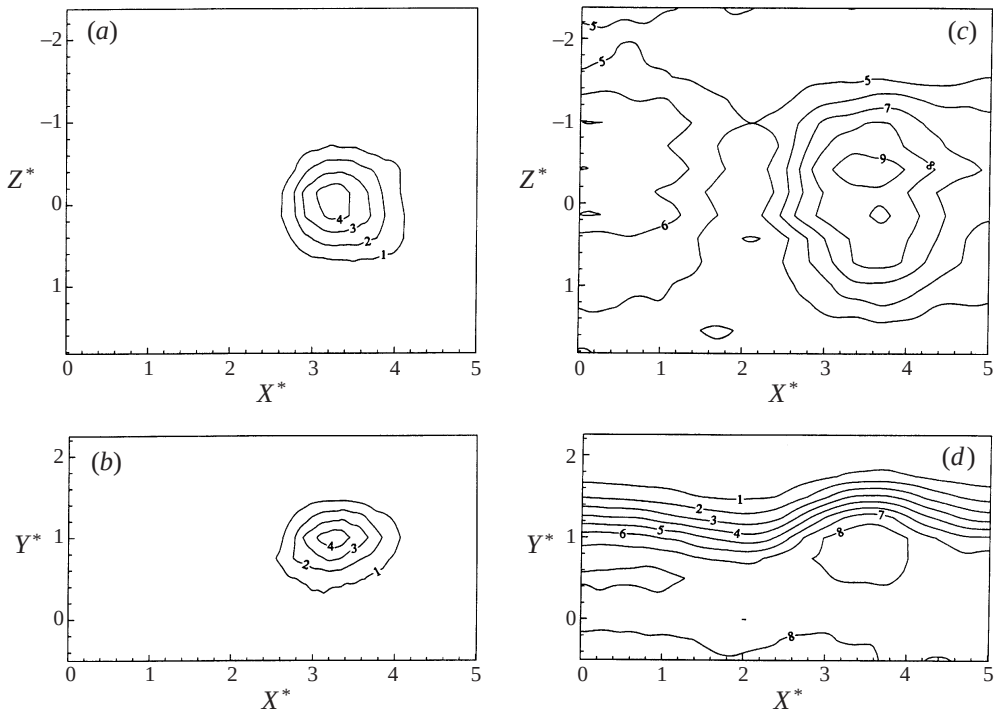

FIGURE 11. Ensemble average of $\langle k^* \rangle^2 \times 100$ in (*a*) the (X^*, Z^*)-plane at $Y^* = 1.0$ and (*b*) the (X^*, Y^*)-plane at $Z^* = -0.14$, and of $\langle k_r^{*2} \rangle \times 100$ in (*c*) the (X^*, Z^*)-plane at $Y^* = 1.0$ and (*d*) the (X^*, Y^*)-plane at $Z^* = -0.14$.

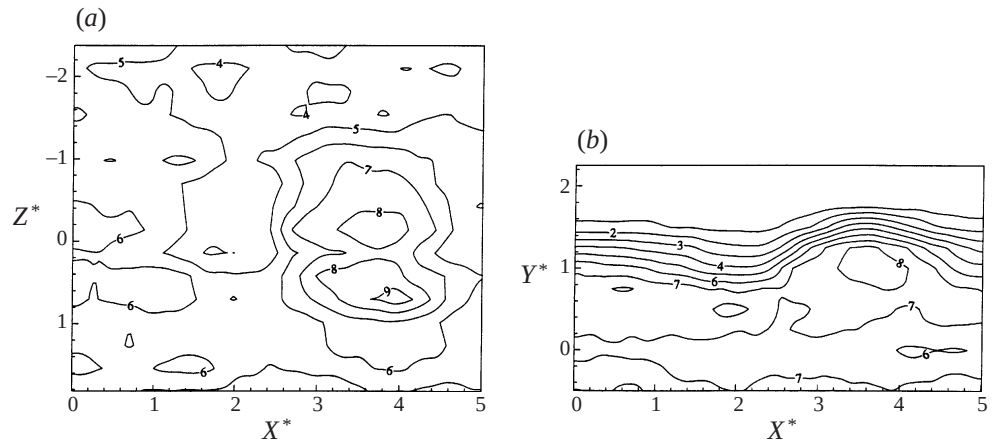

FIGURE 12. Ensemble average of $\langle u_r^{*2} \rangle \times 100$ in (*a*) the (X^*, Z^*)-plane at $Y^* = 1.0$ and (*b*) the (X^*, Y^*)-plane at $Z^* = -0.14$.

reported by Antonia *et al.* (1987). In the horizontal plane, lower values are observed outside the two foci, again in the region where there is colder fluid (Vernet *et al.* 1997).

It has been assumed that the small-scale motions (also called random or incoherent in the literature), calculated from the difference between the total and

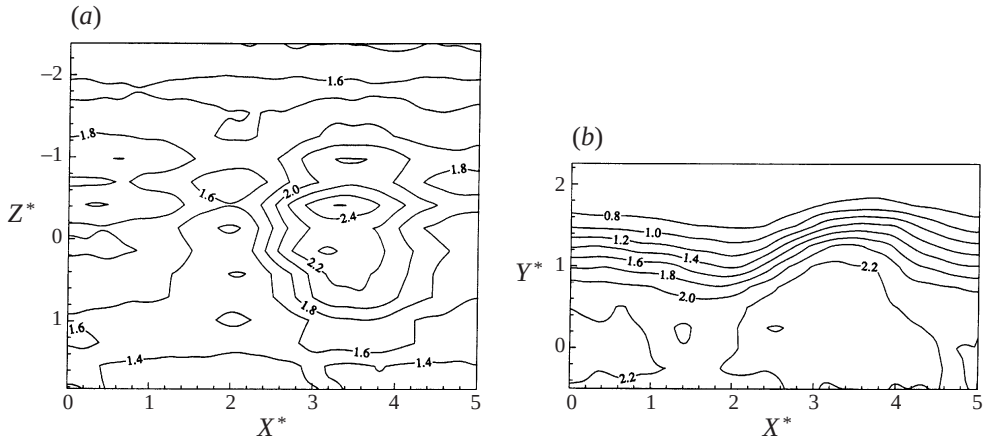

FIGURE 13. Ensemble average of the fine-scale turbulence indicator function (see text) in (*a*) the (X^*, Z^*)-plane at $Y^* = 1.0$ and (*b*) the (X^*, Y^*)-plane at $Z^* = -0.14$.

coherent stresses, are due entirely to the small scales. As pointed out by Antonia *et al.* (1987) and by Ferré *et al.* (1990), fully developed turbulent shear flows have a wide degree of scatter in individual structures due not only to differences in the smaller incoherent scales but also to differences in size, intensity and orientation of the structures. In addition, misclassifications that occur during identification and misalignments during averaging contribute to this scatter. Ferré *et al.* (1990) defined and used a fine-scale turbulence indicator function and found that the stresses due to the small-scale motions, identified in this way, exhibit more scatter in the homogenous plane of the fully developed wake than in the vertical plane. Thus, figure 12 must be viewed with some caution, especially figure 12(*b*), since the topology of the structures is more variable in the horizontal than in the vertical plane.

To better assess how representative $\langle u_r^{*2} \rangle$ is, the contours of the fine-scale turbulence indicator function proposed by Ferré *et al.* (1990) are plotted in figure 13 for the present data. The fine-scale turbulence indicator function is the envelope of the second derivative of velocity with respect to time. The Hilbert Transform is used to find the envelope. It should be noted that this function is biased to the higher frequencies, which may not fully represent the behaviour of the incoherent motions. Nevertheless, the similarity of the isocontours between figures 12 and 13 support in a qualitative way the results for $\langle u_r^{*2} \rangle$ presented in figure 12.

6.3. *Production and dissipation of turbulence*

Hussain (1983) developed the transport equations for a triple decomposition of the velocity field. Figures 14 and 15 depict, respectively, the contours of the shear production of coherent energy,

$$\langle S_c \rangle = -\langle u^* \rangle \langle v^* \rangle \frac{\partial U^*}{\partial Y^*} \tag{20}$$

and shear production of the incoherent energy

$$\langle S_r \rangle = -\langle u_r^* v_r^* \rangle \frac{\partial U^*}{\partial Y^*}. \tag{21}$$

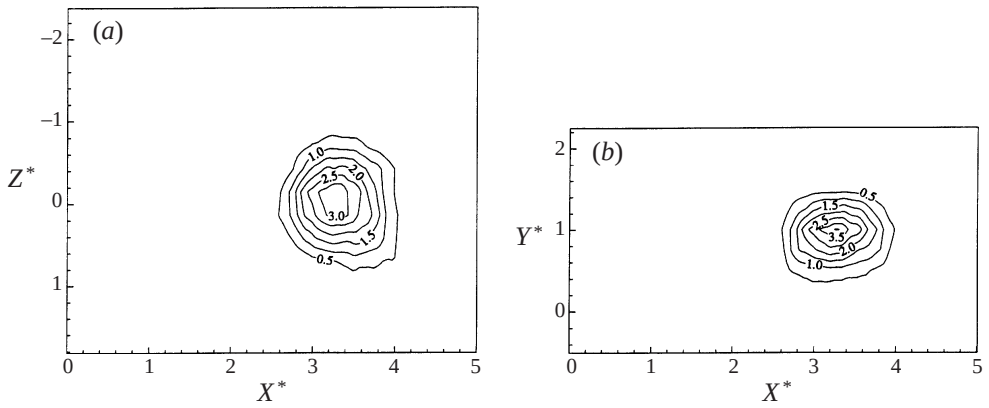

FIGURE 14. Ensemble average of the mean shear production of coherent energy, $\langle S_c \rangle$ (see equation (20)), in (*a*) the (X^*, Z^*)-plane at $Y^* = 1.0$ and (*b*) the (X^*, Y^*)-plane at $Z^* = -0.14$. The contour levels are multiplied by 100.

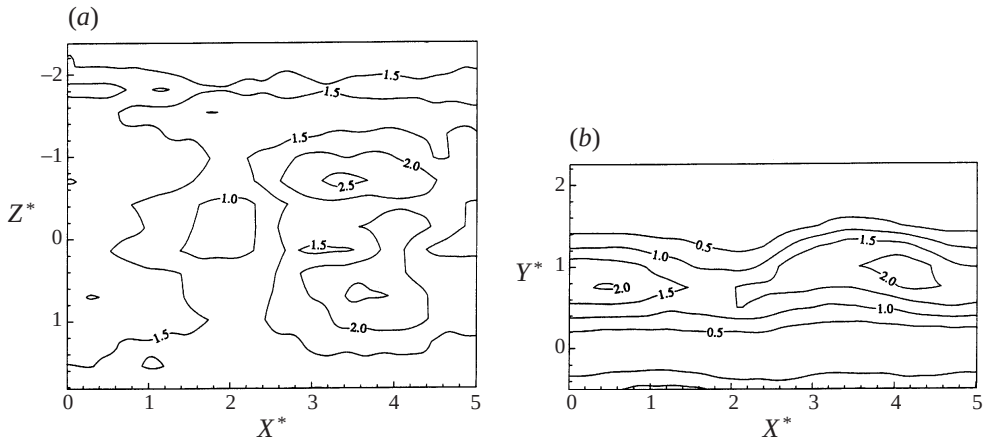

FIGURE 15. Ensemble average of the mean shear production of incoherent energy, $\langle S_r \rangle$ (see equation (21)), in (*a*) the (X^*, Z^*)-plane at $Y^* = 1.0$ and (*b*) the (X^*, Y^*)-plane at $Z^* = -0.14$. The contour levels are multiplied by 100.

The shear production of coherent energy by the mean velocity field is largest between the two foci in the horizontal plane of the structure (figure 14*a*) and in the structure's vertical symmetry plane at $Y^* = 1.0$ slightly below the focus in the vertical plane. This region of maximum production is the mixing jet region of the structure. The lateral, spanwise and streamwise extent of this production term are all of the order of l_0. The comparison between figures 11 and 14 shows that the coherent energy is maximum at the location where it is produced. Thus, a simple eddy viscosity model (e.g. equation (1)) should be able to describe the coherent energy distribution in the wake flow.

Evidently, the coherent structure extracts energy from the mean flow via stretching in the mixing jet region, between the two 'legs' of the ring. Vortex stretching by the mean flow is an effective method for the transfer of energy from the mean field to

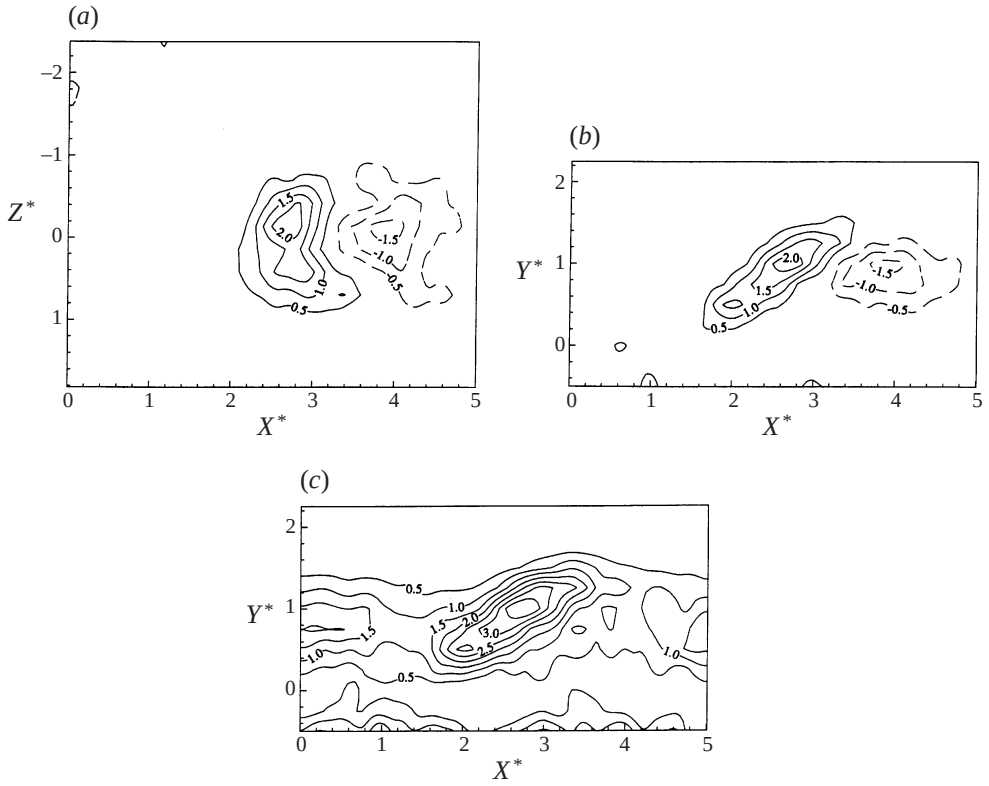

FIGURE 16. Ensemble average of the production of incoherent energy by the coherent motions, $\langle P_r \rangle$ (see equation (22)), in (*a*) the (X^*, Z^*)-plane at $Y^* = 1.0$ and (*b*) the (X^*, Y^*)-plane at $Z^* = -0.14$. (*c*) Ensemble average of the production of incoherent energy (equation (21) + equation (22)) in the (X^*, Y^*)-plane at $Z^* = -0.14$ using the double decomposition. The contour levels are multiplied by 100.

the coherent field since the coherent vorticity is roughly aligned with the mean rate of strain. Because the vortex is inclined in the streamwise direction, vortex stretching by the mean strain works to maintain the correlation between $\langle u^* \rangle$ and $\langle v^* \rangle$. Because of the shape of the vortex, namely a ring as opposed to a single roller, $\langle u^* \rangle$, $\langle v^* \rangle$ and $\langle u^* \rangle \langle v^* \rangle$ must be largest near the symmetry plane of the vortex (i.e. in the mixing jet region). $\langle S_c \rangle$ is also largest in this region.

The shear production of small-scale turbulence energy by the mean velocity field (equation (21)), depicted in figure 15, has a relative deficit at the saddle point (i.e. upstream of the structure) and is largest at about $Y^* = 1.0$, away from the symmetry plane of the structure but between the two foci of the double roller motions. Therefore, the production is, in this case, largest outside the mixing jet region but still between the two foci observed in the horizontal plane. Thus, the incoherent and coherent motions extract energy from the mean flow at different locations with respect to the structure. The peak value of $\langle S_r \rangle$ in figure 15 is about 70% of that for $\langle S_c \rangle$ in figure 14, but is spread over a larger area. Certainly the total production of each term is of the same order of magnitude.

Figure 16 shows the contours of the production of the small-scale energy by the

coherent motions (Hussain 1983),

$$\langle P_r \rangle = -\langle u_r^{*2} \rangle \frac{\partial \langle u^* \rangle}{\partial X^*} - \langle v_r^{*2} \rangle \frac{\partial \langle v^* \rangle}{\partial Y^*} - \langle w_r^{*2} \rangle \frac{\partial \langle w^* \rangle}{\partial Z^*} - \langle u_r^* v_r^* \rangle \left(\frac{\partial \langle v^* \rangle}{\partial X^*} + \frac{\partial \langle u^* \rangle}{\partial Y^*} \right) - \langle u_r^* w_r^* \rangle \left(\frac{\partial \langle u^* \rangle}{\partial Z^*} + \frac{\partial \langle w^* \rangle}{\partial X^*} \right), \tag{22}$$

where we have neglected the term involving $\langle v_r^* w_r^* \rangle$ because no simultaneous lateral and spanwise velocity measurements have been made in the present study. It is suspected that this term is quite small because the coherent strain rate $\partial \langle w^* \rangle / \partial y^* + \partial \langle v^* \rangle / \partial z^*$ is also small.

The contours of $\langle P_r \rangle$ in figure 16 are well-organized and less randomized than the production of small-scale energy by the mean field, $\langle S_r \rangle$ (figure 15), even though both terms involve similar small-scale stresses. It is observed that in the vertical plane $\langle P_r \rangle$ is largest near the saddle point at the upstream end of the mixing jet region but upstream of the coherent vortex, consistent with the results of Antonia *et al.* (1987). The peak values occur near (2.5, 0.7, 0) and are equal in magnitude to those for the other production terms (equations (20) and (21) in figures 14 and 15). The production drops abruptly to zero at the saddle point and is shear-aligned below it. Peak values occur in the symmetry plane.

It is also interesting to note that negative production occurs in the mixing jet region where the incoherent streamwise stress, $\langle u_r^{*2} \rangle$ (figure 12*a*), is maximum as is the incoherent turbulence kinetic energy. Clearly, incoherent turbulence is produced in a different region from where it occurs, indicating that simple eddy viscosity or local models such as equation (1) will not work well for the prediction of the incoherent turbulence terms in the transport equations.

This negative production of incoherent turbulence appears to be due to newly engulfed fluid moving inwards from the spanwise edges of the structure. In this way, the engulfed/entrained fluid contributes to the maintenance of the coherent structures. This should not be mistaken for energy transfer from the fine scales to the large scales, but should rather be viewed as an effect of the bulk (coherent) motions. In this case it means a transfer from the incoherent to coherent turbulence. This would be consistent with the view of negative production put forward by Beguier *et al.* (1977). Finally, this negative production also means that there is little direct transfer between the coherent and incoherent turbulent motions.

Figure 16(*c*) shows the total production of incoherent energy when a double decomposition is applied. This figure is shown for comparison with the results of Antonia *et al.* (1987). The contours are in close agreement indicating that the structures identified are similar. Note that in the present work more terms are included (equation (22)) because the date are three-dimensional.

Figure 17 depicts the ensemble average of the one-component energy dissipation rate

$$\varepsilon = \left\langle \left(\frac{\partial u_r^*}{\partial X^*} \right)^2 \right\rangle. \tag{23}$$

The contours in the vertical symmetry plane are similar to those of Antonia *et al.* (1987), although the peak magnitude obtained here is more than one order of magnitude larger due to differences in the frequencies of the low-pass filter and sampling rates used (Vernet 1997). It is observed that the peak values are downstream of the saddle within the mixing jet region. Thus, production and dissipation of the

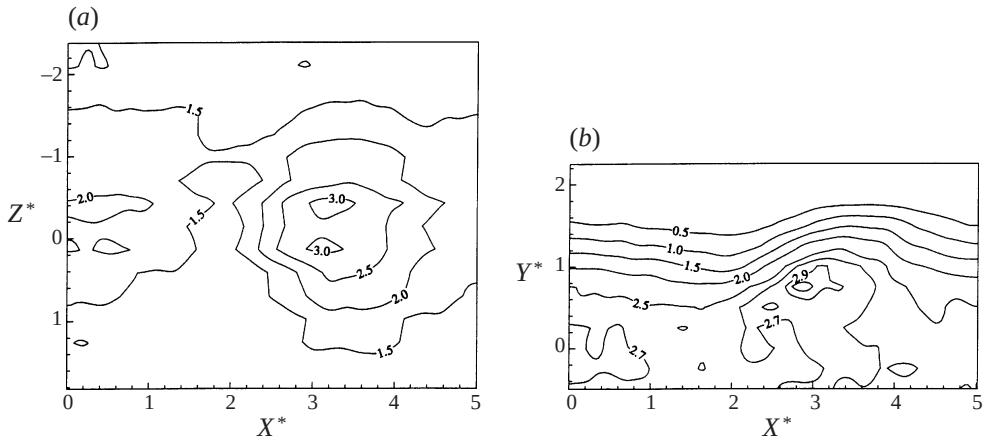

FIGURE 17. One-component dissipation, $\langle(\partial u^*/\partial X^*)^2\rangle$, in (*a*) the (X^*, Z^*)-plane at $Y^* = 1.0$ and (*b*) the (X^*, Y^*)-plane at $Z^* = -0.14$.

small scales both occur in the mixing jet region but the largest values of dissipation occur just between the positive and negative production shown in figure 16 at what is the upstream edge of the structure.

6.4. *Entrainment*

Townsend (1976) proposed a 'growth–decay' cycle of entrainment for plane turbulent wakes. Groups of entrainment eddies, which grow out of the main turbulent motion, cause large bulges and indentations of the initially quiescent turbulent–non-turbulent interface to grow. The bulges finally overturn causing large-scale engulfment. Townsend differentiates the eddies of the main turbulent motion, which are double rollers, from the entrainment eddies, which have spanwise vorticity. The present work suggests that the entrainment eddies and double rollers are different aspects of the ring-like vortex structure.

The strong outward lateral velocities that exist in the centre of the ring in the mixing jet region cause the bulges to grow. The indentations are accentuated by the inward velocities upstream of the ring-like vortex, just upstream of the saddle point. Coherent and incoherent turbulence is produced in the mixing jet region, between the two foci of the double rollers. This fine-scale turbulence is ejected outwards toward the edge of the wake. It should be noted that the indentations do not extend down to the saddle point which is embedded in the turbulent flow since the intermittency factor is near unity at $Y^* = 1$.

Antonia *et al.* (1987) pointed out that the incoherent motions (or stresses) do not concentrate in the foci of the vortex structures in the far wake, unlike in the near-wake region. From the present results, it seems likely that the incoherent turbulence produced within the mixing jet region does not have time to be transported into the focus at the top of the ring structure. For example, from figure 3 it is estimated that for a fluid particle within the mixing jet region to move to the vortex centre requires a path of approximately $3l_0$. Using the largest ensemble-averaged velocity fluctuation identified, it would take a particle more than 800 ms to move $3l_0$. During this time the entire structure would have been convected more than $500D$ downstream. The structure certainly would have evolved in this time. Thus, it seems more reasonable

that the incoherent turbulence is ejected outwards, to the edge of the wake, as part of the growth–decay cycle.

7. Conclusions

The average three-dimensional structure of the velocity fluctuations, obtained by identifying temperature transitions in the (X^*, Z^*)-plane at $Y^* = 1.0$, is a shear-aligned ring-shaped vortex. This vortex structure is characterized by strong outward v- and negative u-velocity fluctuations in its centreplane region and by an upstream saddle point. Grant's mixing jet occurs between the two foci of the double rollers as part of the ring. The mixing jet extends outside the vortex, however, all the way to the upstream saddle point. When a double decomposition is used, the prototypical coherent structure is found to be a tube-shaped vortex with a spanwise extent of about $2.5l_0$.

The turbulence kinetic energy, production by coherent motions, production by the mean field and the (one-component) dissipation rate are highly three-dimensional processes which occur primarily within the mixing jet region. These processes do not completely overlap, however.

The bulk of the turbulence kinetic energy of the ring vortex is associated with the incoherent velocity fluctuations. It is, however, the coherent field which organizes the incoherent turbulence. The production of small-scale energy by the coherent motions and the one-component energy dissipation rate both occur near the saddle point located at the upstream end of the mixing jet outside the structure boundary while the production of incoherent energy by the mean field occurs slightly further downstream and outside the mixing jet but between the two foci of the double rollers. There is negative production of incoherent turbulence at the downstream end of the mixing jet region which is likely to be due to the bulk convective motions of the coherent structure. This should not be regarded as a transfer from the fine scales to the large scales. Thus, the momentum transfer processes do not overlap and the peak levels of incoherent energy are separated in space from the regions where it is produced. The coherent structure also extracts enrgy from the mean flow within the mixing jet region. The spanwise extent of all these processes is about l_0.

Two-equation turbulence models tend to work well in free shear flows such as plane turbulent wakes in spite of the relative complexity of the transfer processes observed in this 'simple' flow. This complexity includes the fact that the incoherent turbulence (i) does not exist in the same region as it is produced and (ii) contributes to the production of coherent turbulence. The reason why these models function well in simpler flows may be because there is very little net transfer between the coherent and incoherent motions, leaving primarily transfer from the mean flow. In the far region of a plane turbulent wake, this occurs over a single length scale. It seems likely that when a significant strain is placed on a flow such as a turbulent wake, the relative magnitudes of turbulence production are shifted, owing to the structural changes which occur (e.g. Kopp & Keffer 1996). In this case there will be different net transfer between the mean flow and the coherent and incoherent motions. In these situations the turbulence models tend to fail.

This work was financially supported by DGICYT projects PB91-0551 and PB96-1011, NATO Collaborative Research Grant 960142, and NSERC. The hardware and a portion of the software were supported by PB93-0656-C02-01. Computer support

was granted by the Servei de Tecnologia Quimica of the Universitat Rovira i Virgili. G. A. Kopp was financially supported by NSERC and Universitat Rovira i Virgili during the course of this investigation carried out in Tarragona.

Appendix. Template dependence of ensemble averages

An additional analysis of the data was done using two alternative templates, namely a colder-to-hotter template and a colder-hotter-colder template. This analysis was performed in order to check if the velocity field results obtained with the hotter-to-colder template are template dependent or whether they represent different motions. Figure 18(*a*) shows the colder-to-hotter template while figure 19(*a*) shows the colder-hotter-colder template. From the 72 files analysed an average of 574 temperature events were selected, accounting for 40% of the recorded data when figure 18(*a*) was used and an average of 414 temperature events when figure 19(*a*) was used. The standard deviation of the number of temperature events selected is 44 and 23, while the mean and standard deviation of temperature maxima are 1.54 and 0.04 and 1.49 and 0.01, respectively. This compares favourably to the values presented in the main body of the text where 592 events, with a standard deviation of 32 events, were identified. These had a mean value of the maximum temperature of 1.51 with a standard deviation of 0.08. Thus, approximately the same number of events is selected with all three templates. However, the resulting averaged temperature patterns, shown in figures 18(*b*) and 19(*b*) (cf. figure 2*b*), are significantly different in all three cases.

The coherent velocities are depicted in figures 18(*c*, *d*) and 19(*c*, *d*) and vorticity contours in figures 18(*e–g*) and 19(*e–g*). These should be compared with those in figures 3 and 6. In spite of the strong template dependence of the temperature averages, the velocity patterns are essentially the same in appearance, but with some differences in the precise details.

The first impression when looking at the results is that the basic patterns are the same, but are just shifted within the windows. This first impression is accurate, but there are some differences. First, the size of the patterns is largest in the colder-hotter-colder pattern. In fact, the final temperature pattern is essentially just a hotter spot of larger scale than the two other 'gradient' templates where the original temperature transitions remained intact. Although one would expect a colder-hotter-colder template to be more constraining than either the hotter-to-colder or colder-to-hotter templates, the converged pattern is less restrictive and probably has much more smearing associated with it, judging by the larger size of the patterns. This implies that the spacing between structures, when they occur in groups (e.g. those identified by Antonia *et al.* 1987), varies from group to group so that when a prescribed spacing is not set, only the hotter pattern associated with the mixing jet region of the coherent structure is finally identified with the pattern recognition technique.

A second observation is that the upstream or downstream saddle point is more clearly defined depending on which of the two gradient-type templates is chosen. This makes sense because the hotter fluctuations are correlated with negative streamwise velocity fluctuations while the colder fluctuations are correlated with positive velocity fluctuations. Thus, where there are temperature 'fronts' there is a high probability of a saddle point. (However, a saddle point is not always observed; see for example, Kopp *et al.* 1997.) When the different templates are used, different temperature fronts are selected for averaging so that slightly different velocity patterns are obtained.

Figures 18(*h*, *i*) and 19(*h*, *i*) show the incoherent energy production by the coherent

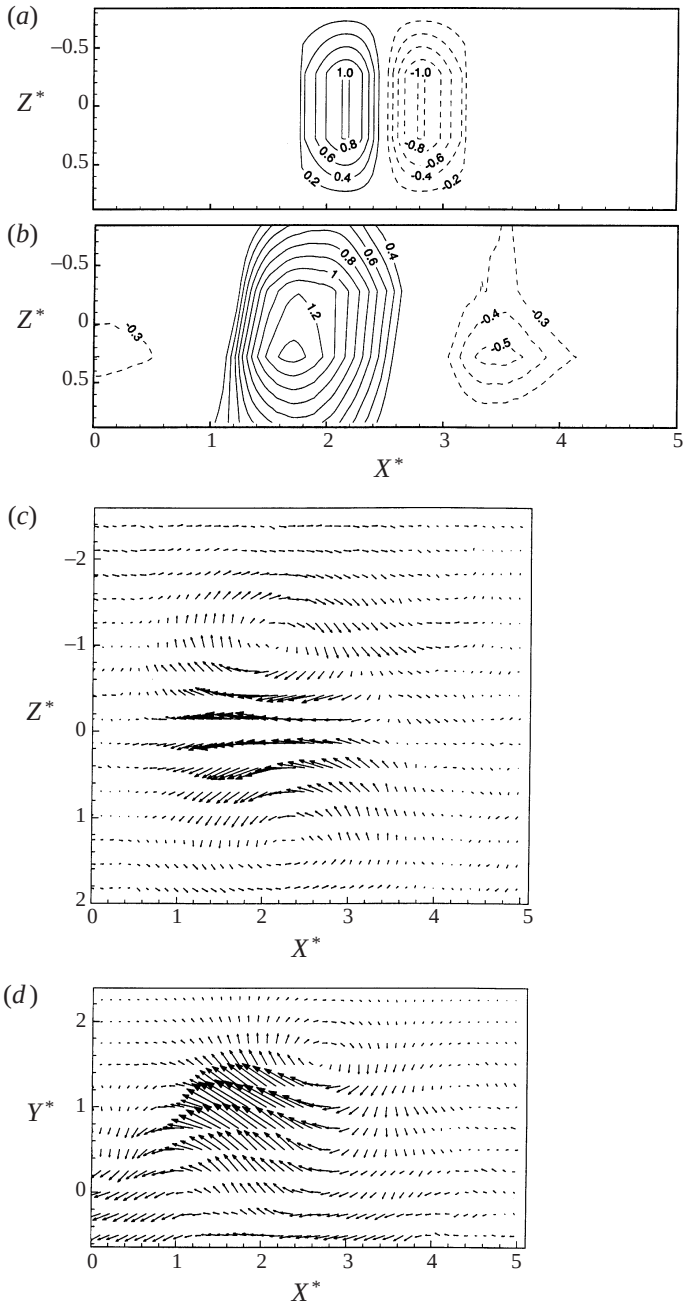

FIGURE 18 (*a–d*). For caption see facing page.

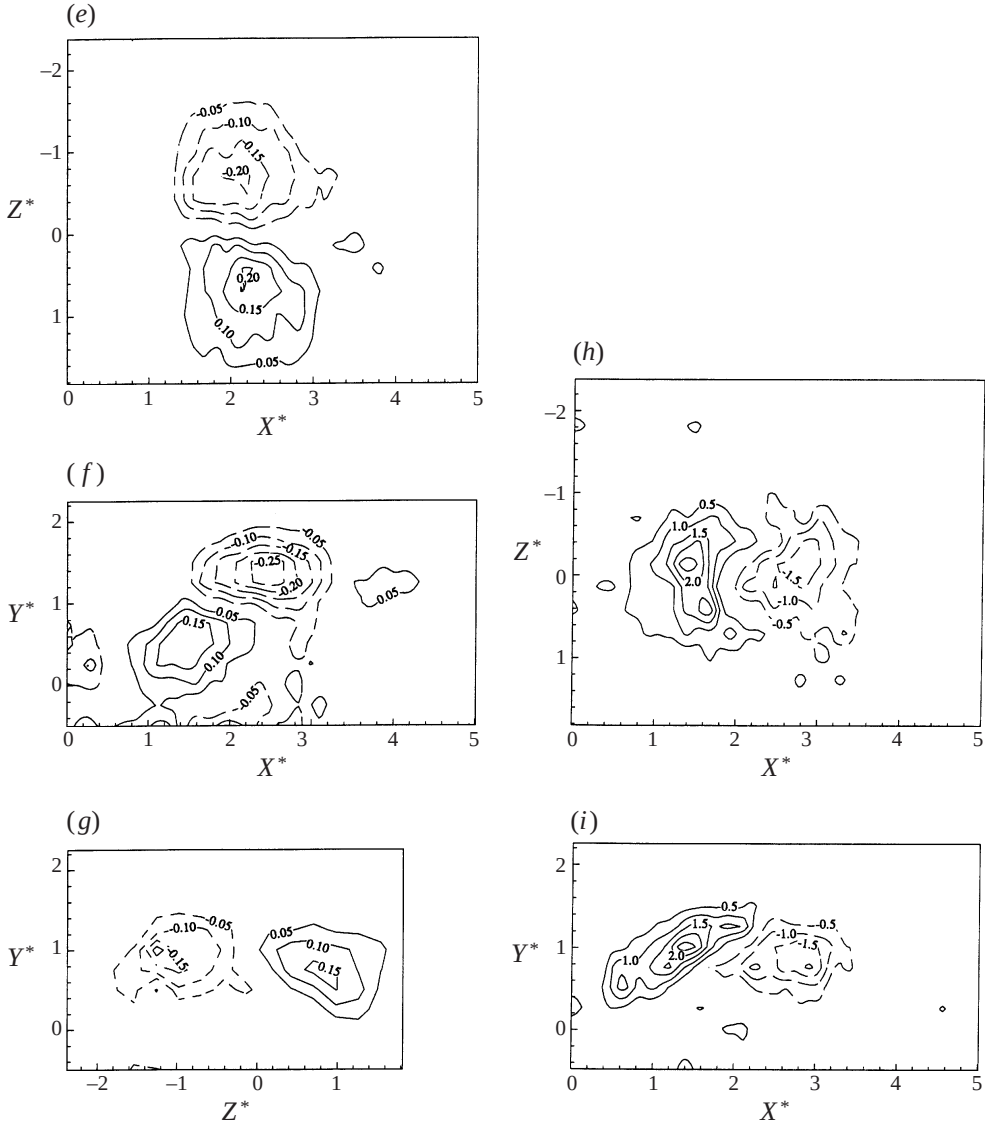

FIGURE 18. (*a*) Colder-to-hotter temperature template, and ensemble averages of (*b*) $\langle\theta^*\rangle$ in the (X^*, Z^*)-plane at $Y^* = 1.0$, (*c*) $(\langle u^*\rangle, \langle w^*\rangle)$ in the (X^*, Z^*)-plane at $Y^* = 1.0$, (*d*) $(\langle u^*\rangle, \langle v^*\rangle)$ in the (X^*, Y^*)-plane at $Z^* = -0.14$, (*e*) $\langle\omega_y\rangle$ in the (X^*, Z^*)-plane at $Y^* = 1.0$, (*f*) $\langle\omega_z\rangle$ in the (X^*, Y^*)-plane at $Z^* = -0.14$, (*g*) $\langle\omega_x\rangle$ in the (Y^*, Z^*)-plane at $X^* = 2.1$ and the ensemble average of the production of incoherent energy by the coherent motions, $\langle P_r\rangle$ (multiplied by 100), in (*h*) the (X^*, Z^*)-plane at $Y^* = 1.0$ and (*i*) the (X^*, Y^*)-plane at $Z^* = -0.14$.

motions (using the triple decomposition). These can be compared with figure 16. Clearly, the three patterns obtained from the three templates show the same topology. Most of the production occurs at the upstream end of the mixing jet region. Therefore, the production occurs physically closest to the location of the hotter-to-colder temperature transition and the 'upstream' saddle point, as observed in figures 3, 6 and 16. The other contours occupy slightly more space, possibly indicating more smearing in the averages. The peak values are similar, however.

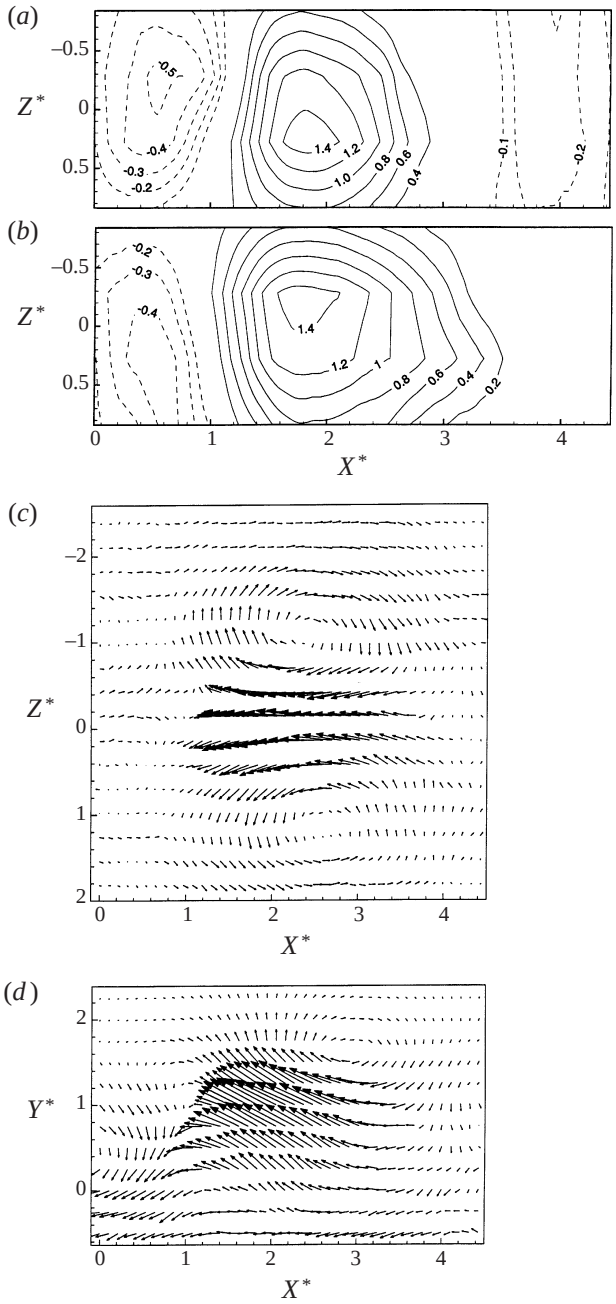

FIGURE 19 (*a–d*). For caption see facing page.

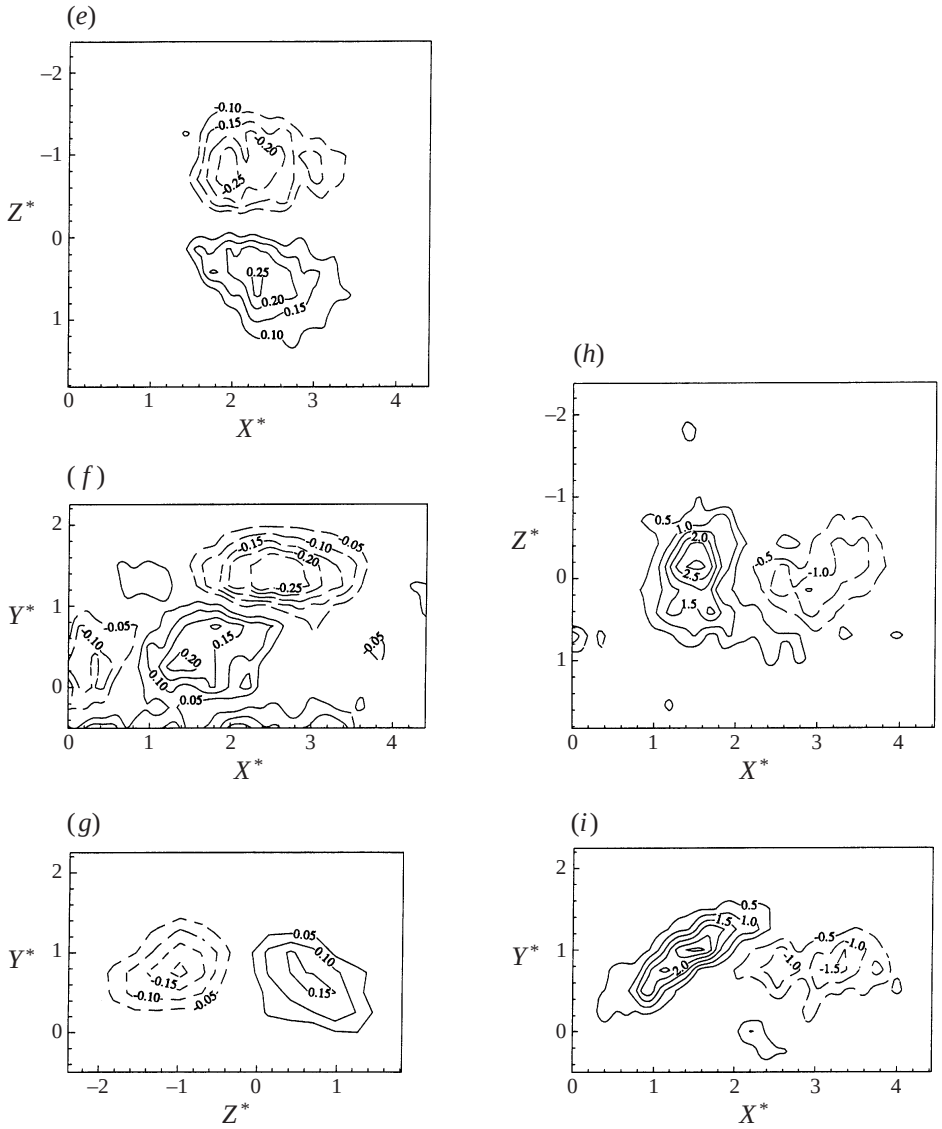

FIGURE 19. As figure 18 but for the colder-hotter-colder template; and in (*g*) $X^* = 2.4$.

In summary, the ensemble-averaged structures obtained by using a hotter-to-colder template and a colder-to-hotter template are nearly the same. There are some features within the ensemble averages which depend on template, in particular the upstream and downstream saddle points. Results based on the hotter-to-colder template have been chosen for the main body of the paper because much of the physics of momentum transfer occurs closest to the colder-to-hotter temperature transition and the coincident saddle point. A colder-hotter-colder template is not able to identify the upstream and downstream saddle points simultaneously because of variable spacing between adjacent structures.

REFERENCES

Antonia, R. A., Browne, L. W. B., Bisset, D. K. & Fulachier, L. 1987 A description of the organized motion in the turbulent far wake of a cylinder at low Reynolds number. *J. Fluid Mech.* **184**, 423–444.

Beguier, C., Giralt, F., Fulachier, L. & Keffer, J. F. 1977 Negative production in turbulent shear flows. In *Structure and Mechanisms of Turbulence II* (ed. H. Fiedler). *Lecture Notes in Physics*, vol. 76, pp. 22–35. Springer.

Bisset, D. K., Antonia, R. A. & Browne, L. W. B. 1990 Spatial organization of large structures in the turbulent far wake of a cylinder. *J. Fluid Mech.* **218**, 439–461.

Chong, M. S., Perry, A. E. & Cantwell, B. J. 1990 A general classification of three-dimensional flow fields. *Phys. Fluids* A **2**, 765–777.

Cimbala, J. M., Nagib, H. M. & Roshko, A. 1988 Large structure in the far wakes of two-dimensional bluff bodies. *J. Fluid Mech.* **190**, 265–298.

Ferré, J. A. & Giralt, F. 1989*a* Pattern-recognition analysis of the velocity field in plane turbulent wakes. *J. Fluid Mech.* **198**, 27–64.

Ferré, J. A. & Giralt, F. 1989*b* Some topological features of the entrainment process in a heated turbulent wake. *J. Fluid Mech.* **198**, 65–77.

Ferré, J. A., Mumford, J. C., Savill, A. M. & Giralt, F. 1990 Three-dimensional large-eddy motions and fine-scale activity in a plane turbulent wake. *J. Fluid Mech.* **210**, 371–413.

Ferre-Gine, J., Rallo, R., Arenas, A. & Giralt, F. 1997 Extraction of structures from turbulent signals. *Artificial Intell. Engng* **11**, 413–419.

Gieseke, T. J. & Guezennec, Y. G. 1993 Stochastic estimation of multipoint conditional averages and their spatio-temporal evolution. In *Eddy Structure Identification in Free Turbulent Shear Flows* (ed. J. P. Bonnet & M. N. Glauser), pp. 281–292. Kluwer.

Giralt, F. & Ferré, J. A. 1993 Structure and flow patterns in turbulent wakes. *Phys. Fluids* A **5**, 1783–1789.

Grant, H. L. 1958 The large eddies of turbulent motion. *J. Fluid Mech.* **4**, 149–190.

Guezennec, Y. G. 1989 Stochastic estimation of coherent structures in turbulent boundary layers. *Phys. Fluids* A **1**, 1054–1060.

Hayakawa, M. & Hussain, F. 1989 Three-dimensionality of organized structures in a plane turbulent wake. *J. Fluid Mech.* **206**, 375–404.

Hunt, J. C. R., Wray, A. A. & Moin, P. 1988 Eddies, stream and convergence zones in turbulent flows. *Center for Turbulence Research Rep.* CTR-S88, pp. 193–208.

Hussain, A. K. M. F. 1983 Coherent structures – reality and myth. *Phys. Fluids* **26**, 2816–2850.

Hussain, A. K. M. F. & Hayakawa, M. 1987 Eduction of large-scale organized structures in a turbulent plane wake. *J. Fluid Mech.* **180**, 193–229.

Jeong, J. & Hussain, F. 1995 On the identification of a vortex. *J. Fluid Mech.* **285**, 69–94.

Kaplan, W. 1958 *Ordinary Differential Equations.* Addison-Wesley.

Keffer, J. F. 1965 The uniform distortion of a turbulent wake. *J. Fluid Mech.* **22**, 135–159.

Kopp, G. A., Ferré, J. A. & Giralt, F. 1997 The use of pattern recognition and proper orthogonal decomposition in identifying the structure of fully-developed free turbulence. *Trans. ASME*: *J. Fluids Engng* **119**, 289–296.

Kopp, G. A., Kawall, J. G. & Keffer, J. F. 1995 The evolution of the coherent structures in a uniformly distorted plane turbulent wake. *J. Fluid Mech.* **291**, 299–322.

Kopp, G. A. & Keffer, J. F. 1996 Coherent structures in two uniformly distorted plane turbulent wakes. *Phys. Fluids* **8**, 2706–2711.

Libby, P. A. 1976 Prediction of the intermittent turbulent wake of a heated cylinder. *Phys. Fluids* **19**, 494–501.

Meiburg, E. & Lasheras, J. C. 1988 Experimental and numerical investigation of the three-dimensional transition in plane wakes. *J. Fluid Mech.* **190**, 1–37.

Moser, R. D., Rogers, M. M. & Ewing, D. W. 1998 Self-similarity of time-evolving wakes. *J. Fluid Mech.* **367**, pp. 255–289.

Mumford, J. C. 1983 The structure of the large eddies in fully developed turbulent shear flows. Part 2. The plane wake. *J. Fluid Mech.* **137**, 447–456.

Payne, F. R. & Lumley, J. L. 1967 Large eddy structure of the turbulent wake behind a circular cylinder. *Phys. Fluids* **10**, S194–S196.

Taneda, S. 1959 Downstream development of wakes behind cylinders. *J. Phys. Soc. Japan* **14**, 843–848.

Theodorsen, T. 1952 Mechanism of turbulence. In *Proc. 2nd Midwestern Conf. Fluid Mech., Ohio State Univ., Columbus.*

Townsend, A. A. 1956 *The Structure of Turbulent Shear Flow*. Cambridge University Press.

Townsend, A. A. 1976 *The Structure of Turbulent Shear Flow*, 2nd Edn. Cambridge University Press.

Vernet, A. 1997 Analisi de la naturalesa de les estructures coherents en l'estela llunyana d'un cilindre. PhD thesis (in Catalan), Universitat Rovira i Virgili, Tarragona, Spain.

Vernet, A., Kopp, G. A., Ferré, J. A. & Giralt, F. 1997 Simultaneous velocity and temperature patterns in a homogeneous plane of a cylinder-generated turbulent far wake. *Trans. ASME*: *J. Fluids Engng* **119**, 493–496.

Wygnanski, I., Champagne, F. & Marasli, B. 1986 On the large-scale structures in two-dimensional, small-deficit, turbulent wakes. *J. Fluid Mech.* **168**, 31–71.

Zhou, Y. & Antonia, R. A. 1992 Convection velocity measurements in a cylinder wake. *Exps. Fluids* **13**, 63–70.